Master of Science Dissertation:

Perfusion MRI: Non-Linear Stochastic Regularization for Deconvolution of Model-Free Arterial Spin Labelling Data

André Ahlgren

Supervisors:

Linda Knutsson
Ronnie Wirestam

Abstract

Introduction: Arterial spin labelling (ASL) is a non-invasive magnetic resonance imaging (MRI) technique for assessment of perfusion. ASL uses magnetically labelled blood water as a diffusible endogenous tracer to measure the perfusion of brain tissue, i.e. the cerebral blood flow (CBF). Traditionally, ASL samples images at a specific point in time allowing the CBF to be calculated using a model of the signal. With time-resolved ASL, perfusion-weighted images are sampled as a function of time, allowing the CBF to be calculated using a model-free approach by means of deconvolution. The QUASAR ASL implementation employs this approach and has previously been used to calculate CBF through deconvolution with block-circulant singular value decomposition (cSVD) resulting in slightly lower perfusion values than those achieved with gold standard methods (such as PET). The use of non-linear stochastic regularization (NSR) for deconvolution has previously been investigated, showing good potential to reproduce realistic tissue residue functions in contrast-agent-based perfusion studies by dynamic susceptibility contrast MRI (DSC-MRI). The NSR method gives the possibility to correct for arterial dispersion and therefore potentially improve the perfusion quantification. In this study, NSR was applied as a deconvolution method for absolute quantification of CBF using time-resolved ASL data obtained by the QUASAR pulse sequence. The aim was primarily to see if the implementation was feasible for ASL data, and secondly to assess the potential of improving the absolute CBF quantification and the retrieved residue functions in ASL experiments.

Materials and Methods: Data originated from volunteers participating in a multi-centre reproducibility study of QUASAR. The imaging was carried out with a Philips Achieva 3T MRI unit using the following protocol: 7 slices, 6 mm slice-thickness, 2 mm slice gap, 64×64 matrix, 240×240 mm^2 FOV, 35°/11.7° flip angles, TR/TE/ΔTI/TI$_1$ = 4000/23/300/40 ms, 13 inversion times, 84 series, 2.5 SENSE factor, 150 mm labelling thickness, 3.75×3.75 mm^2 in-plane resolution and a total scantime of 6 min. To obtain the data required for the deconvolution, the acquired ASL image data were post-processed using in-house-developed software, with some additions and modifications compared to previous post-processing software from the QUASAR studies. The most important addition was the implementation of a fractional segmentation and a subsequent novel method to calculate the equilibrium magnetization of arterial blood, which is an essential parameter that directly scales the CBF. To make use of NSR with ASL data, some modifications compared to the available NSR software for DSC-MRI data was needed. One of the main modifications was to model the high measurement noise generally immanent to ASL.

Results and Discussion: The implementation resulted almost consistently in smooth, physiologically realistic residue functions. Especially compared to the most common model-free deconvolution method, cSVD, the resolved residue functions had significantly more physiologically realistic characteristics, primarily regarding monotonic decrease, non-negative values and, consequently, no oscillations. Visual inspection of reconvolved tissue signals served as a qualitative validation, and indicated that the method was able to solve a variety of different kinetic signals. The absolute quantification of CBF in grey matter did not differ from previous methods and resulted in problems with under- and overestimations in certain voxels. This could partially be explained by the fact that NSR tends to fail if the measured signal is too noisy in a voxel, whereas, for example, cSVD produces a potentially false but non-zero result for those voxels. However, the new implementations of fractional segmentation and estimation of the equilibrium magnetization of arterial blood proved to have the potential to reduce CBF quantification errors due to partial volume effects and the presence of non perfused volumes (e.g., CSF).

Conclusion: The implementation of NSR on QUASAR data was successful and encouraging results were obtained. Resolved residue functions showed more realistic characteristics than what is normally achievable with common deconvolution methods. However, the resulting CBF values did not appear to be more realistic than those obtained using previous deconvolution methods. NSR as a deconvolution method for ASL is likely to require substantial verification and optimization to be considered a complement to the already existing methods.

Table of contents

1 Introduction

1.1 Blood flow to the brain

The importance of the delivery of blood to the human brain has been known for centuries (Hill, 1896). Early studies on the anatomy of the cerebral vasculature and the cerebral circulation laid the very basis for succeeding studies of the delivery of blood to the brain tissue. Constant upholding of this blood supply is vital to the homeostasis of the brain tissue since the blood delivers oxygen and nutrients. The process of the delivery of oxygenated blood to the capillary bed of tissue is called perfusion and the cerebral blood flow (CBF) is the measurable physical quantity of the perfusion of the brain. Figure 1.1 shows an example of a CBF map in a brain slice. The CBF is often presented in units of ml/100g/min and is thus a volumetric flow rate.
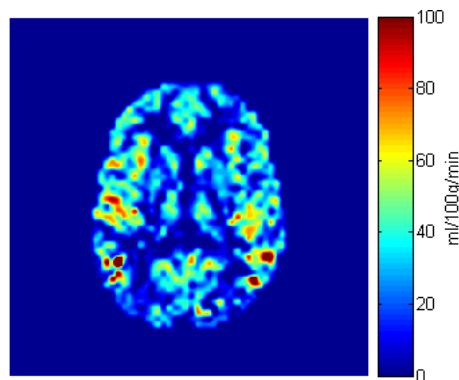

Figure 1.1: Measurement of regional CBF is often displayed as a 2D map of the perfusion. This allows the specialist physician (e.g. radiologist or clinical neurophysiologist) to perform a visual evaluation of the perfusion in different tissues and regions of the brain.

Since the perfusion of the brain is vital, the measurement of CBF is of great clinical importance. Firstly, the generation of quantitative maps of regional CBF can be used to identify areas with vascular disorders, e.g., a decreased CBF due to an ischaemic stroke. Furthermore the coupling between CBF and metabolism makes the quantification a possible marker of brain function which has led to a multitude of studies investigating the connection between an abnormal regional CBF and the diagnostics and prognostics of different disorders, such as neurodegenerative diseases.

Kety and Schmidt were the first scientists to describe a technique to accurately measure quantitative CBF (Traystman, 2004). They adopted Fick's principle and posed that the amount of an inhaled, diffusible and inert gas, taken up by the brain tissue, is equivalent to the amount of the gas that is delivered to the brain by arterial

blood minus the amount that is carried away by venous blood (Kety and Schmidt, 1945). The subjects inhaled nitrous oxide until steady-state and the CBF was estimated from the changes in the arterial and venous concentrations of the tracer. Their reported global mean CBF level of 54 ± 12 ml/100g/min in healthy young men (Kety and Schmidt, 1948) is still regarded to be a quite reasonable value.

In the following decades, other methods for quantitative measurement of CBF have been developed, mainly in the areas of single photon emission computerized tomography (SPECT), positron emission tomography (PET), computerized tomography (CT) and magnetic resonance imaging (MRI). The methods differ in the tracer agents applied, where SPECT uses photon emitting tracers like ^{133}Xe, PET makes use of positron emitting tracer compounds such as $H_2^{15}O$,^{18}F-fluoromethane or ^{77}Kr, dynamic perfusion CT uses non-ionic iodinated contrast agents and Xe-CT stable xenon, while dynamic susceptibility contrast MRI (DSC-MRI) and dynamic contrast enhanced MRI (DCE-MRI) employs chelates of gadolinium(III) as intravenously injected contrast agents and arterial spin labelling (ASL) is based on the use of magnetically labelled blood-water as an endogenous tracer. Almost all methods employ a modelling of the tracer kinetics (the contrast agent transport in tissue) to quantify the CBF, usually either with compartment models or some version of the indicator dilution theory, as developed by Meier and Zierler (Zierler, 1962).

1.2   Aims of the present study

Arterial spin labelling has been used for perfusion quantification of the brain since its introduction in 1992 (Detre et al., 1992; Williams et al., 1992), and has since then advanced in many different ways and directions. Most ASL implementations model the MR signals and use different assumptions to obtain regional CBF (i.e., a CBF map). Recently, an ASL pulse sequence capable of measuring the MR signal at multiple points in time made CBF quantification possible with much fewer assumptions (Petersen et al., 2006a). This sequence is called "Quantitative STAR labelling of Arterial Regions" (QUASAR) and in this approach the time-resolved ASL data are used to calculate kinetic tracer data which allows for quantification of the perfusion by means of deconvolution. Since the implementation does not utilize any modelling of the signals, it is often called model-free ASL. The QUASAR reproducibility study resulted in a mean grey matter CBF of 47.4 ml/100g/min which is in the lower end of published values obtained using ASL techniques and quite low compared to gold standard methods such as PET (Leenders et al., 1990).

Deconvolution is a mathematical operation which is far from straightforward, and the result from such an operation can depend on the selected methodology. Petersen et al. used a deconvolution method called block-circulant singular value decomposition (cSVD). However, cSVD has been shown to have limited accuracy since obtained CBF values depend on dispersion (i.e., broadening) of the arterial bolus signal and on a threshold value applied to limit the effects of noise, and also since it produces physiologically unrealistic solutions (i.e., non-monotonically

decreasing with negative values). We hypothesized that a better suited deconvolution technique could improve the perfusion quantification with model-free ASL. Non-linear stochastic regularization (NSR) is a deconvolution technique developed specifically to respect the generally smooth characteristics of the physiological signals in DSC-MRI (Zanderigo et al., 2009), and the present study aimed to implement and adapt NSR to serve as a deconvolution method in model-free ASL. We also present a novel method for estimation of the equilibrium magnetization of arterial blood, which is an essential parameter for the perfusion quantification in ASL.

2 Theory

2.1 Introduction to perfusion quantification with bolus-tracking

This section gives a brief introduction to the basics of bolus-tracking perfusion quantification which is essential to the following theory. As will be seen later, perfusion quantification with model-free ASL can be interpreted in a very similar manner.

Kety and Schmidt measured the concentration of a freely diffusible tracer in arterial and venous blood to calculate CBF. Another method to quantify brain perfusion is to use bolus-tracking of a tracer transversing the microvascular system. With bolus-tracking, the CBF is often calculated through the indicator-dilution theory proposed by Meier and Zierler (Zierler, 1962). The indicator dilution theory describes the passage of a tracer through the microvasculature by means of dynamic functions. The individual tracer particles follow different paths through the microvasculature and their transit times therefore have a distribution with a shape depending on the flow and the vascular structure. The transport function $h(t)$ is the probability distribution function of these transit times given an ideal bolus injection (an infinitely short tracer-bolus injected into the tissue-feeding vessel at the entrance of the capillary network). Since $h(t)$ is a probability distribution, the integral over all transit times equals unity:

$$\int\limits_0^\infty h(\tau)\, d\tau = 1 \qquad\qquad 2.1$$

The residue function $R(t)$ is the fraction of tracer still present in the microvasculature at time t after the ideal bolus injection. Since $\int_0^t h(\tau)\, d\tau$ is the total fraction of tracer that has left the microvasculature at time t, the residue function can be formulated as:

$$R(t) = 1 - \int\limits_0^t h(\tau)\, d\tau \qquad\qquad 2.2$$

The definition of $h(t)$ implies that $R(t)$ is a monotonically decreasing and non-negative function equal to unity at time zero and converging to zero as time approaches infinity. The shape of $h(t)$, and therefore $R(t)$, is characteristic for the system and the tracer (Zierler, 1965). Figure 2.1 displays the relationship between $h(t)$ and $R(t)$.
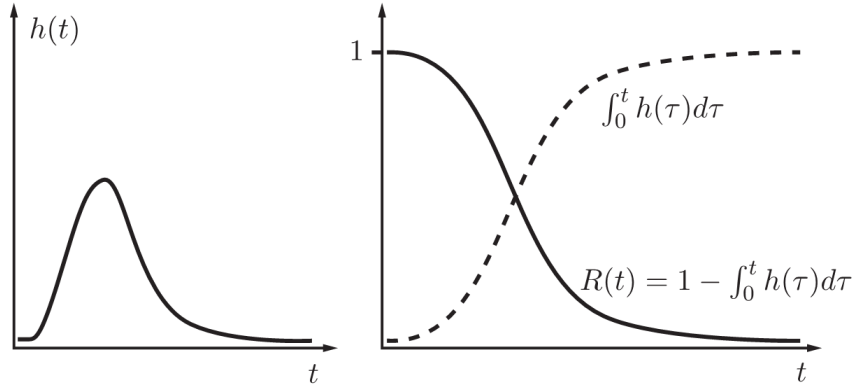
Figure 2.1: The relation between $h(t)$ and $R(t)$.

Since the rate of the injection is finite, and due to bolus broadening when traversing the circulatory system from the site of injection (typically a peripheral vein) to the brain, the tracer bolus will not be an ideal delta function in reality and the so-called arterial input function $AIF(t)$ is the course of tracer concentration in the tissue-feeding artery entering the microvasculature at time t. By using time-domain impulse functions, and assuming a time-invariant and linear system, the course of tracer concentration $C(t)$ in tissue can be described as (Zierler, 1962):

$$C(t) = CBF \cdot AIF(t) \otimes R(t) = CBF \cdot \int_0^t AIF(\tau) \cdot R(t-\tau) \, d\tau \qquad 2.3$$

where $\otimes$ is the convolution operator and the right-hand side is the convolution integral. Figure 2.2 displays a graphical example of Eq. 2.3. The tissue signal $C(t)$ is the output of the system, the arterial input function is the input to the system, and the residue function is the characteristic of the system and the tracer, also known as the convolution kernel (e.g., $CBF \cdot R(t)$). Hence, $CBF \cdot R(t)$ can be obtained by deconvolution of the measured time courses $C(t)$ and $AIF(t)$, and the CBF can be calculated as the initial height of $CBF \cdot R(t)$ since $R(0) = 1$. It is obvious that a unique $CBF \cdot R(t)$ needs to be determined in every voxel to obtain a regional CBF map like the one in Figure 1.1. The true AIF at the entrance of the capillary system is sometimes dispersed (broadened or smeared out) compared to the AIF actually measured at another site, resulting in an apparent, dispersed residue function (e.g., not monotonically decreasing). Therefore, the CBF is often estimated as the maximum of $CBF \cdot R(t)$ instead of the value at time zero and it is clear that this leads to underestimated CBF if dispersion effects are present.
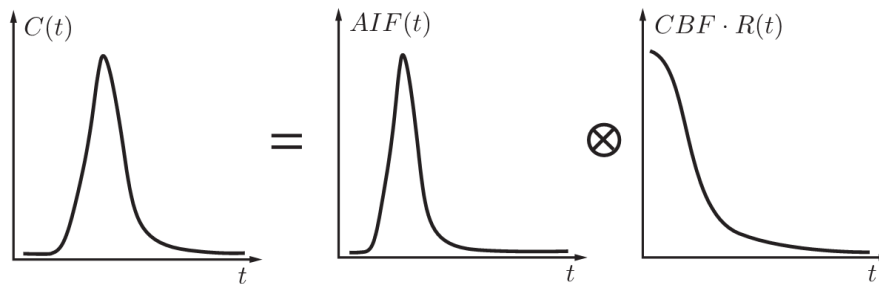
Figure 2.2: The measured tissue signal is the realization of a convolution between the arterial input function and the residue function, multiplied by the CBF.

2.2   Basic principles of arterial spin labelling

The basis for ASL, or arterial spin tagging, was laid in 1992 by the joint efforts of Donald Williams, John Detre, John Leigh and Alan Koretsky (Detre et al., 1992; Williams et al., 1992). They showed that saturation or inversion (labelling) of arterial spins induces a measurable change in the longitudinal magnetization of tissue downstream, and that this change can be used to quantify the perfusion of the brain. It should be noted that Kwong and colleagues independently showed that the change of apparent tissue relaxation time, also due to an inversion, can be used to quantify perfusion (Kwong et al., 1992), although their research focused more on neural activation which is beyond the scope of this thesis.
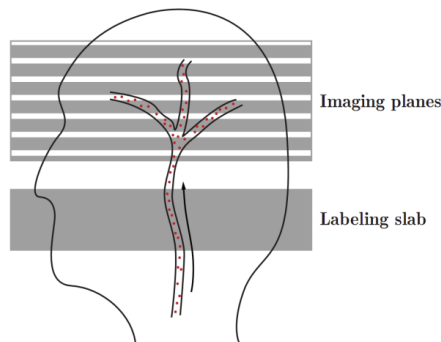
Figure 2.3: Schematic figure of the basic ASL experiment. The ascending arterial blood is inverted and shortly after, when the labelled blood reaches the brain tissue, the imaging is initiated.

Arterial spin labelling uses magnetically labelled blood water as an endogenous, diffusible tracer to measure small changes in the longitudinal magnetization (signal), due to the inflow and blood-tissue exchange (through the blood-brain barrier) of labelled blood-water. In its most simple form the idea is to label (invert or saturate)

6

arterial blood-water in a slice proximal to the imaging plane, wait until the labelled blood has reached the imaging plane and the blood water has exchanged with tissue, perform the image read-out and then repeat the process but without labelling the arterial blood, thus producing a reference called control image. Figure 2.3 displays the concept of labelling arterial blood on its way to the brain. The difference image resulting from subtracting the labelled image from the control image reflects the regional CBF and by constructing a model of this magnetization difference a quantitative CBF map can be extracted. A large number of different ASL techniques exist and all of them cannot be derived here. It seems, however, appropriate to briefly explain the different main branches of ASL since they can exhibit both methodological and theoretical differences. Traditionally, ASL is divided into two groups of experiments, namely continuous ASL (CASL) and pulsed ASL (PASL).

The first ASL experiment in rats by Williams and colleagues (Detre et al., 1992; Williams et al., 1992) is pertained to the CASL methods where arterial blood is continuously labelled proximal to the imaging plane until a steady state is reached in the tissue magnetization. The labelling employs so-called continuous flow-driven adiabatic inversion which is performed by applying a 2-4 s continuous radiofrequency (RF) pulse with a magnetic field gradient in the flow direction. This will saturate static tissue while the spins that move in the gradient direction will be inverted due to the variation in resonance frequency. The labelling also gives rise to unwanted off-resonance saturation of the pool of bound protons in brain tissue macromolecules, which due to cross-relaxation mechanisms affects the pool of free protons and thus the image signal. This magnetization transfer effect must be reproduced in the control experiment to avoid any contribution from static tissue in the difference image. This can be accomplished in various ways, and Williams and colleagues used a distal labelling outside the rat head, with labelling and control slices placed symmetrically on each side of the imaging plane. Such an approach is only valid for a single slice half-way between the labelling and control slices, and a better solution is to use double adiabatic inversion (Alsop 1998), which employs two adjacent inversion planes, thus returning the traversing spins to the original non-inverted state. Williams and colleagues also suggested the use of gradients (Williams 1992) to minimize signal contribution from flowing spins in large vessels (thus eliminating signal originating from macroscopic flow, i.e., not perfusion).

In pulsed ASL, first suggested 1994 by Edelman et al. (Edelman et al., 1994), the labelling is performed with a temporally short inversion pulse (5-20 ms) over an extended volume (i.e., a thick slice). Figure 2.4 shows the basic idea of a PASL experiment. The control image must still be compensated for the magnetization transfer effects, and this can be achieved by using two subsequent inversion pulses of half the RF power. This first PASL sequence named "Echo-Planar Imaging and Signal Targeting with Alternating Radiofrequency" (EPISTAR) has spawned sequences such as STAR-HASTE, PULSAR and QUASAR. A conceptually different PASL sequence is "Flow Alternating Inversion Recovery" (FAIR) (Kim, 1995; Kwong et al., 1995) in which the spin population of a slice in the imaging plane is inverted and then the spins of the whole brain are inverted for the control

image. These different sequences are nicely reviewed by Petersen et al. (Petersen et al., 2006b).

In addition, a hybrid method called pseudocontinuous ASL (pCASL) has recently emerged (Wu et al., 2007). This approach uses repeating short (pulsed) RF pulses to label by flow-driven adiabatic inversion like CASL. The method has proven to be very useful since it can exploit the higher tagging efficiency of PASL and the higher SNR of CASL, without the need of continuous RF transmission.
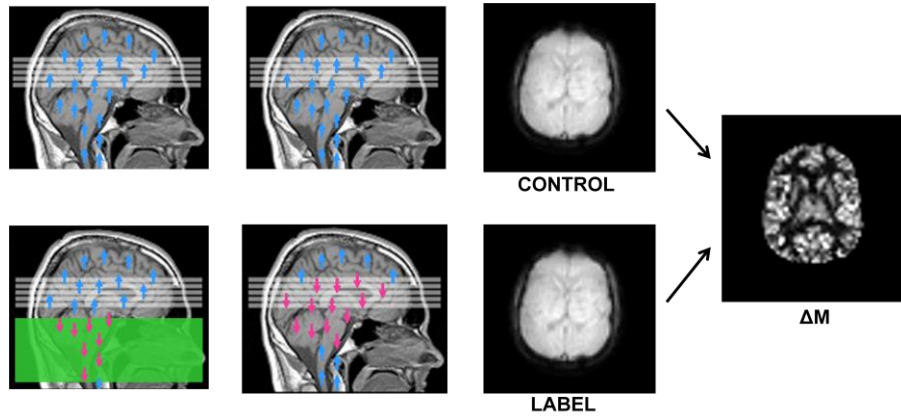

Figure 2.4: By inverting spins proximal to the imaging plane and subtracting the resulting image from a control image with no effective labelling, the difference image is obtained. This difference is called ΔM and it can be used to calculate the tissue perfusion. Images describes a PASL experiment and comes from (Petersen et al., 2006b).

2.2.1 Perfusion quantification in ASL

Williams and colleagues described the change in brain tissue magnetization, with respect to the inflow and outflow of labelled blood, by means of a modified Bloch equation:

$$\frac{dM_t(t)}{dt} = \frac{M_{0,t} - M_t(t)}{T_{1t}} + CBF \cdot \left(M_a(t) - M_v(t)\right) \qquad 2.4$$

where M_t is the tissue magnetization, $M_{0,t}$ is the equilibrium tissue magnetization, T_{1t} is the longitudinal relaxation time of tissue and M_a and M_v is the magnetization of arterial and venous blood, respectively. This is a direct adaption of the tracer clearance theory developed by Kety and Schmidt (Kety and Schmidt, 1948). As steady state is reached, the label and control images are registered and the perfusion can be calculated by solving the differential equation. Improved versions of this model have later been introduced.

In 1998 Buxton et al. (Buxton et al., 1998) proposed the use of a general kinetic model to describe the magnetization difference ΔM (i.e., the difference in signal between the label and the control images):

$$\Delta M(t) = 2 \cdot M_{0,a} \cdot CBF \cdot \int_0^t c(\tau) \cdot r(t - \tau) \cdot m(t - \tau) \, d\tau \qquad 2.5$$

where $M_{0,a}$ is the equilibrium magnetization in arterial blood, $c(t)$ is the fractional input function describing the delivery of labelled spins entering the microvasculature, $r(t)$ is the fractional wash-out function corresponding to spins leaving the microvasculature, and $m(t)$ is the fractional longitudinal relaxation function describing the relaxation of labelled spins. This formulation is similar to the indicator dilution theory (cf. Eq. 2.3) although ASL uses a diffusible tracer. The model is applicable to any ASL experiment and can be used with different compartment models. Still, the dynamic functions have to be modelled if the CBF is to be quantified from traditional ASL data. In the present study, the QUASAR sequence is employed which describes time-resolved ASL data through the general kinetic model (Eq. 2.5) enabling CBF to be calculated by means of deconvolution instead of modelling (Petersen et al., 2006a).

2.3 Model-free arterial spin labelling

This chapter describes the method of model-free ASL and the MRI sequence QUASAR as suggested and developed mainly by Esben Petersen and Xavier Golay (Petersen, 2009; Petersen et al., 2006a; Petersen et al., 2010).

All ASL approaches are based on modelling the change in longitudinal magnetization due to the inflow and blood-tissue exchange of labelled blood water. The inversion time, i.e. the time between labelling and read-out, has to be chosen carefully in order for most models to be accurate. Model-free ASL, as proposed by Petersen et al. (Petersen, 2009; Petersen et al., 2006a), acquire multiple ASL images at different inversion times, thereby obtaining the signal as a function of time (see Figure 2.5). With the ingenious MRI sequence QUASAR, Petersen and colleagues were able to sample dynamic functions and calculate the CBF using a model-free approach by means of deconvolution. Figure 2.5 displays how QUASAR provides the difference in magnetization between label and control, ΔM, as a unique dynamic signal in every voxel. The implementation was evaluated in 284 healthy volunteers in a multi-center reproducibility study (Petersen et al., 2010).
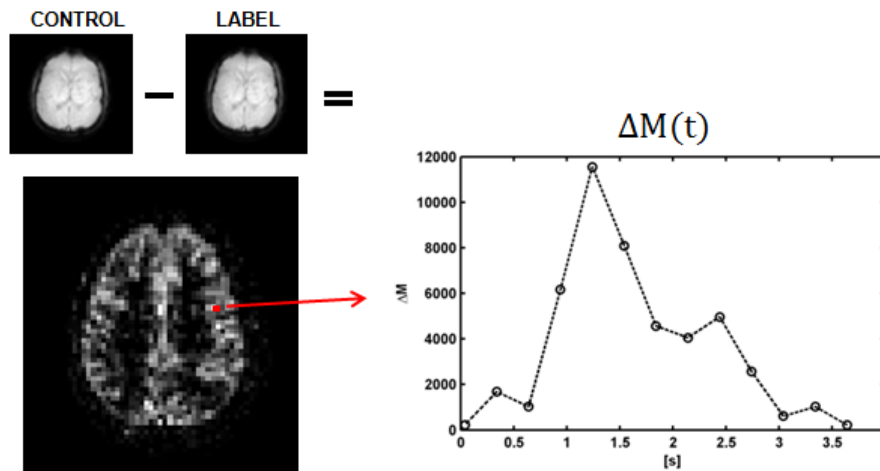
Figure 2.5: In model-free ASL, all images are acquired at multiple points in time allowing the exploitation of dynamic signals.

The QUASAR sequence is a combination of the PULSAR labelling (Golay et al., 2005), Look-Locker readout (Look and Locker, 1970) and Q2-TIPS bolus saturation (Luh et al., 1999). The PULSAR labelling consists of an initial four-pulse saturation which minimizes the signal from static tissue, lowering the noise in the difference image, followed by a modified EPISTAR labelling and a subsequent saturation pulse for a clean start of the bolus, similar to QUIPSS I (Wong et al., 1998). The readout uses a multi-slice, single-shot, gradient-echo EPI sequence combined with a small flip angle to allow sampling with a high temporal resolution (Look-Locker sampling strategy). Bolus saturation is also applied just proximal to the imaging plane before each slice acquisition to ensure a well-defined end of the bolus (Q2-TIPS). Bipolar crusher (spoiler) gradients can be used to null the signal from large arteries (Ye et al., 1997) and the QUASAR sequence exploits this by repeating the entire experiment with and without crusher gradients. By subtracting the crushed signal from the non-crushed signal, the shape of the AIFs can be acquired (see Figure 2.6). The crushed signal is used when calculating ΔM to ensure that the CBF is not overestimated due to signal contribution from inflowing arterial blood (vascular artifacts). The experiment is also repeated with a lower flip angle to allow mapping of B_1-inhomogeneities (spatial variations of the excitation RF field) and slice selection effects.

Petersen et al. exploited the sampled dynamic perfusion signal together with sampled arterial input functions and directly applied the general kinetic model proposed by Buxton et al. (Buxton et al., 1998). Using notations similar to traditional bolus-tracking experiments (cf. Eq. 2.3) the general kinetic model (Eq. 2.5) can be written as (Petersen 2006a):

$$\Delta M(t) = CBF \cdot \int_0^t AIF(\tau) \cdot R(t - \tau) \, d\tau \qquad\qquad 2.6$$

where $AIF(t) = 2 \cdot M_{0,a} \cdot c(t)$, $2M_{0,a}$ is the magnetization difference and $R(t - \tau) = r(t - \tau) \cdot m(t - \tau)$ is the effective residue function, i.e. the combined effects of the wash-out and relaxation of labelled spins. $M_{0,a}$ is the equilibrium magnetization in arterial blood as described earlier.

Model-free ASL is quite unique in utilizing a bolus-tracking approach with a diffusible tracer, with characteristics somewhere in between the bolus-tracking methods using intravascular tracers and the tracer clearance methods using diffusible tracers. This is important to keep in mind when interpreting the theory as well as the results. Since ASL uses a diffusible tracer, the transit times of spins that exhibit blood to tissue to blood exchange are in the order of several minutes and the clearance $r(t)$ will be a slowly decreasing function of time. However, the relaxation of the labelled spins $m(t)$ will occur fast (T_1 of arterial blood and tissue is ~1.5 s at 3T) resulting in a rapid decrease of $R(t)$. It is obvious that the characteristic that traditionally is called the residue function corresponds to $r(t)$ in model-free ASL. However, in this paper $R(t)$ will be referred to as the residue function. Note that this does not compromise the definition of the residue function as a monotonically decreasing function, and that the perfusion still is calculated from $CBF \cdot R(t)$ since no spins have relaxed at time zero, i.e., $m(0) = 1$, and hence $R(0) = 1$. The arterial input function is also different from the traditional definition. Instead of only describing the tracer concentration at the entrance of the capillary system, it actually has to consider the amount of magnetization that is available in arterial blood at the site of the studied capillary system.

2.3.1 Arterial input function and arterial blood volume

As mentioned above, the shape of the AIF can be obtained by subtracting the difference signal curve from the noncrushed data with the difference signal curve from the crushed data, i.e., $\Delta M_{ncr}(t) - \Delta M_{cr}(t)$. See Figure 2.6 for a visual description of this method. The arterial blood volume (aBV) is the fraction of a voxel that consists of arterial blood. This quantity can be calculated with QUASAR by comparing the area under the local AIF with the initial bolus area from the labelling:

$$aBV = \frac{\int_{-\infty}^{\infty} \left(\Delta M_{ncr}(t) - \Delta M_{cr}(t) \right) e^{t/T_{1a}} \, dt}{2 \cdot M_{0,a} \cdot \tau_b \cdot \alpha} \qquad\qquad 2.7$$

where T_{1a} is the longitudinal relaxation time in arterial blood, τ_b is the temporal length of the initial bolus, known through the bolus saturation, and α is the inversion efficiency, i.e. the fraction of the achieved inversion in the labelling plane. Figure 2.7 shows a graphical interpretation of Eq. 2.7.
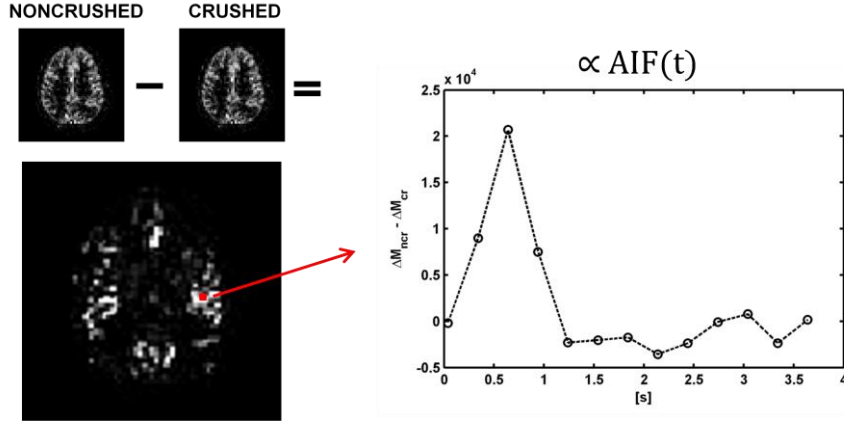
Figure 2.6: The basic idea of obtaining the dynamic of the AIF by subtracting a vascular crushed ΔM_{cr} from a normal acquisition with no crusher gradients ΔM_{ncr}.
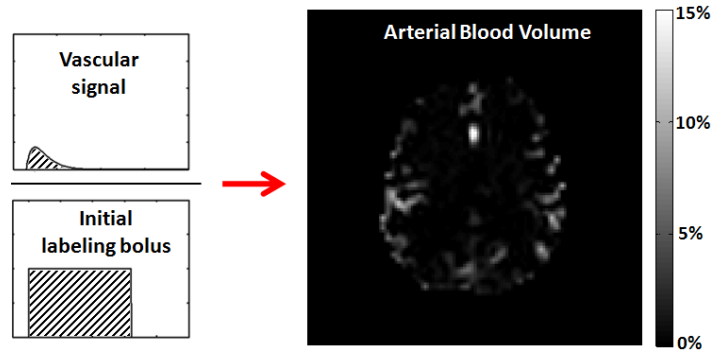

Figure 2.7: The arterial blood volume is calculated by dividing the area under the local vascular signal corrected for relaxation (unique for every voxel), by the initial bolus area at the site of the labelling.

The label will experience multiple saturation pulses due to the Look-Locker readout between the arterial arrival time τ_a and the arrival to the microvasculature at time τ_m. To correct for this, the AIF should be multiplied by $cos^n \phi$, where the number of saturation pulses is given by $n = floor((\tau_m - \tau_a)/\Delta TI)$, ΔTI is the time between the excitation pulses and ϕ is the flip angle ($floor(x)$ is the largest integer not greater than x). Finally, scaling to the correct aBV fraction and accounting for relaxation, $AIF(t)$ can be calculated by:

$$AIF(t) = \frac{\left(\Delta M_{ncr}(t) - \Delta M_{cr}(t)\right) e^{t/T_{1a}}}{aBV} \cdot cos^n \phi \cdot e^{-(t+(\tau_m - \tau_a))/T_{1a}} \qquad 2.8$$

where the last exponential corrects for relaxation of arterial blood between the time of arrival to the site of the AIF and to the microvasculature. To couple with Eq. 2.6,

the AIF can equivalently be calculated as the normalization of the fractional input function $c(t)$:

$$AIF(t) = 2 \cdot M_{0,a} \cdot \alpha \cdot \cos^n \phi \cdot c(t) \qquad 2.9$$

where

$$c(t) = \frac{\left(\Delta M_{ncr}(t) - \Delta M_{cr}(t)\right) e^{t/T_{1a}}}{\int_{-\infty}^{\infty} \left(\Delta M_{ncr}(t) - \Delta M_{cr}(t)\right) e^{t/T_{1a}} \, dt} \cdot e^{-(t+(\tau_m - \tau_a))/T_{1a}} \cdot \tau_b \qquad 2.10$$

Since there is considerable measurement noise in the QUASAR data, a gamma-variate function is fitted to the measured AIF. A unique AIF is then calculated for every voxel, based on the mean of the surrounding AIF curves, the arterial delay, the equilibrium magnetization in arterial blood ($M_{0,a}$) in the current voxel, the number of saturation pulses from the read-out during the vascular transit time ($\tau_m - \tau_a$) and the relaxation of the labelled blood during the same transit time. Figure 2.8 shows examples of maps of the microvascular arrival time τ_m, the arterial arrival time τ_a, the arterial blood volume aBV and the pure blood area (initial bolus at the site of labelling, i.e., the denominator in Eq. 2.7).
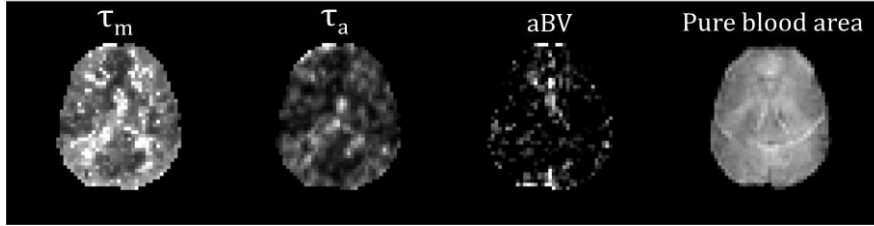

Figure 2.8: Examples of parameters relating to the calculation of the AIF. From left to right: microvascular arrival time τ_m, arterial arrival time τ_a, arterial blood volume aBV and pure blood area.

2.3.2   Brain-blood partition coefficient and $M_{0,a}$

The determination of the magnetization in fully relaxed arterial blood $M_{0,a}$ is of considerable importance since it directly scales the calculated value of the CBF. Traditionally, $M_{0,a}$ has been estimated as a global parameter, obtained from the sagittal sinus. But since the QUASAR sequence enables mapping of the equilibrium magnetization in tissue $M_{0,t}$, $M_{0,a}$ can be estimated on a voxel-by-voxel basis through the brain-blood partition coefficient λ:

$$\lambda = \frac{M_{0,t}}{M_{0,a}} \qquad 2.11$$

The brain-blood partition coefficient can thus be seen as the relation between the proton density of the tissue and the arterial blood. This coefficient is not limited to use in ASL but is generally used to correct for the difference in distribution volume of tracers between blood and tissue (i.e., the ratio of equilibrium tracer concentration

in tissue and blood). Since proton density varies between tissue types, λ varies across the brain. Calculation of $M_{0,a}$ from Eq. 2.11 requires properly determined values of $M_{0,t}$ and λ.

2.3.3 Mapping of M_{0t} and T_{1t}

The use of a Look-Locker sequence to map $M_{0,t}$ and T_{1t} was proposed by Parker et al. (Parker et al., 1998) and was implemented into the QUASAR methodology by Petersen et al. (Petersen, 2009). The raw images from the Look-Locker read-out follow a saturation recovery as the longitudinal relaxation recovers exponentially to a steady-state value (see Figure 2.9 and Figure 2.11).
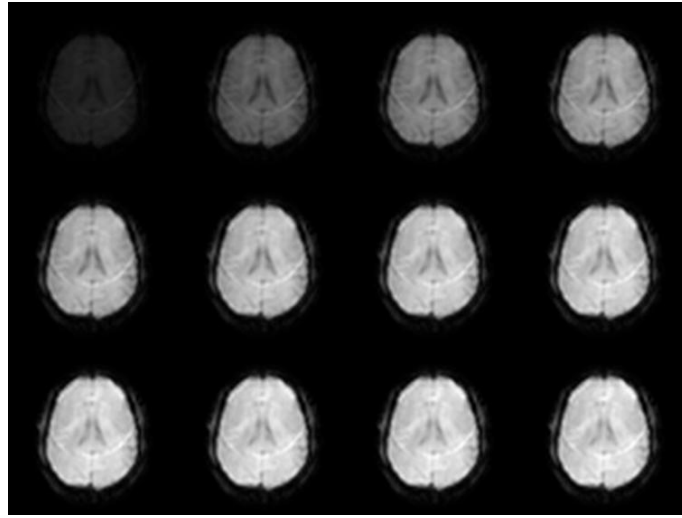

Figure 2.9: Example of raw image data for the 12 first inversion times (left to right order). The successive signal recovery is clearly seen in the images.

The longitudinal magnetization prior to the nth excitation can be expressed through the Bloch equations as:

$$
M_z[n] = M_{0,t} \left(\left(1 + (M_{z+} - 1)e^{-\frac{TI_1}{T_{1t}}} \right) \left(\cos(\phi)e^{-\frac{\Delta TI}{T_{1t}}} \right)^{n-1} \right.
$$

$$
\left. + \left(1 - e^{-\frac{\Delta TI}{T_{1t}}} \right) \frac{1 - \left(\cos(\phi)\, e^{-\frac{\Delta TI}{T_{1t}}} \right)^{n-1}}{1 - \left(\cos(\phi)\, e^{-\frac{\Delta TI}{T_{1t}}} \right)} \right) \qquad 2.12
$$

where M_{z+} is the longitudinal magnetization immediately after excitation, TI_1 is the time between the preparation and the first excitation and ΔTI is the time between the

excitation pulses. The measured signal after the nth excitation pulse will then depend on the longitudinal magnetization just before that excitation:

$$M_{xy}^*[n] = M_z[n] \cdot \sin(\phi) \cdot e^{-TE/T_2^*} \qquad 2.13$$

where the star $(*)$ refers to the non-negligible T_2^* effects in the image (the raw images are primarily proton density weighted). Figure 2.10 displays how the actual signal varies with time, including the effect of the repeated low flip angle excitations.
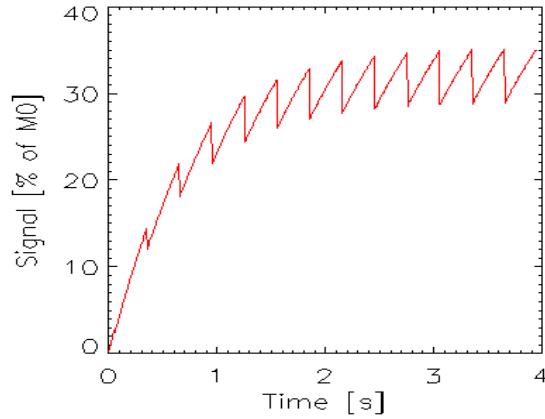

Figure 2.10: The actual signal recovery during the multiple excitations. The signal starts at zero since a saturation (90 degree flip angle) recovery is visualized. The dips correspond to the low flip angle pulses and the values of the peaks are $M_z[n]$ in Eq. 2.12.

The sampled signal course follows an exponential saturation recovery with a limiting value being the effective equilibrium tissue magnetization evaluable through Eq. 2.12:

$$M_{0,t,eff} = \lim_{n \to \infty} M_z[n] = M_{0,t} \cdot \frac{1 - e^{-\frac{\Delta TI}{T_{1t}}}}{1 - \cos(\phi) \, e^{-\frac{\Delta TI}{T_{1t}}}} \qquad 2.14$$

Also, the effective longitudinal relaxation time in tissue can be solved to yield:

$$\frac{1}{T_{1t,eff}} = \frac{1}{T_{1t}} - \frac{\ln(\cos(\phi))}{\Delta TI} \qquad 2.15$$

Both $M_{0,t,eff}$ and $T_{1t,eff}$ can be estimated on a voxel-by-voxel basis by fitting the signal propagation of the raw images to a function on the form:

$$S(t) = M_{0,t,eff} \left(1 - A \cdot e^{-t/T_{1t,eff}}\right) \qquad 2.16$$

where A is a fitting parameter and t is the time after the labelling (inversion time). An example of a measured saturation recovery with a fitted curve can be seen in Figure 2.11. When $M_{0,t,eff}$ and $T_{1t,eff}$ have been estimated, the true $M_{0,t}$ and T_{1t} can be calculated using Eqs. 2.14 and 2.15. However, to avoid significant errors in

$M_{0,t}$ and T_{1t} it is important to take imperfect excitation (inhomogeneous RF field) into account. The correction of the flip angle due to these inhomogeneities will be discussed in the next section.
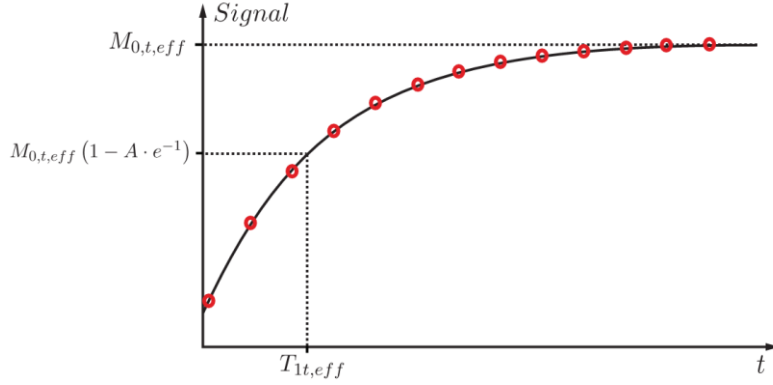

Figure 2.11: The signal recovery is sampled and fitted, allowing the voxel-wise calculation of $M_{0,t,eff}$ and $T_{1t,eff}$.

2.3.4   Mapping of B_1 inhomogeneities and slice-profile effects

One problem with the calculation of $M_{0,t}$ and T_{1t} is that the true flip angle ϕ is needed. The flip angle is often lower than the nominal flip angle due to B_1-field inhomogeneities and slice-profile effects, thus varying across the image. The true flip angle can therefore be defined as the nominal flip angle, multiplied by a correction factor accounting for B_1-field inhomogeneities and slice-profile effects:

$$\phi = \phi_n \cdot g \qquad\qquad 2.17$$

where ϕ_n is the nominal flip angle and g is the correction factor. Petersen et al. employed the dual flip angle strategy (Petersen, 2009), proposed by Parker et al. (Parker et al., 1998), to map g. The slice-profile effects will appear as B_1 variations and will therefore be included in g. Since neither B_1 inhomogeneities nor the true relaxation time of tissue varies with flip angle the use of two different flip angles enables the estimation of g (through Eq. 2.15) by minimizing

$$\frac{1}{T_{1t,eff,low}} + \frac{\ln\bigl(\cos\bigl(\phi_{n,low} \cdot g\bigr)\bigr)}{\Delta TI} - \left(\frac{1}{T_{1t,eff,high}} + \frac{\ln\bigl(\cos\bigl(\phi_{n,high} \cdot g\bigr)\bigr)}{\Delta TI} \right) \qquad 2.18$$

for g. (The slice-profile effects vary with flip angle in a 2D acquisition and this can be accounted for by a correction of g for one of the flip angles.) See Figure 2.12 for an example of a map over the combined B_1 variations and slice-profile effects.
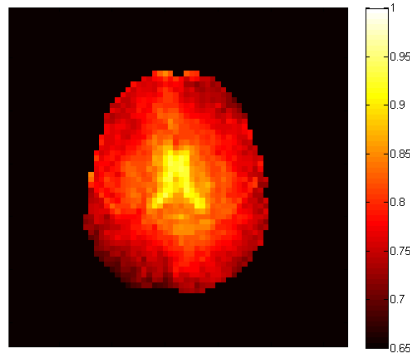
Figure 2.12: The correction factor g mapped in a single brain slice. White color corresponds to an obtained flip angle equal to the nominal. Note that the nominal flip angle is seldom achieved.

When g has been mapped, $M_{0,t}$ and T_{1t} can be calculated with the correct flip angles through Eqs. 2.14 and 2.15. An example of maps of $M_{0,t}$ and T_{1t} is shown in Figure 2.13. In previous implementations of QUASAR, maps of $M_{0,a}$ were calculated by dividing $M_{0,t}$ by λ using one of a few different methods. The following two chapters (2.4 and 2.5) will introduce a new method for this calculation and for mapping of $M_{0,a}$.
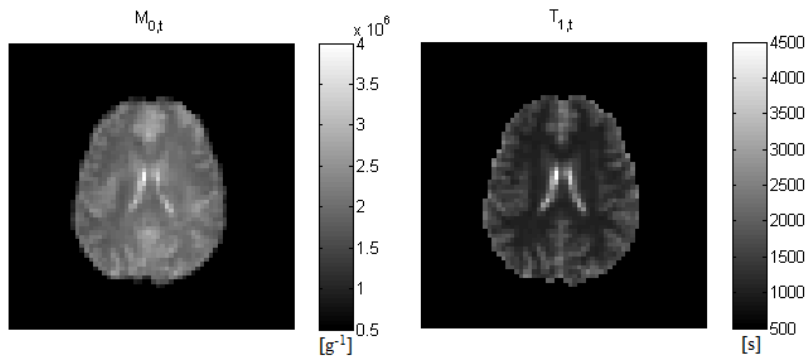
Figure 2.13: Example of calculated parameter maps for $M_{0,t}$ and T_{1t}. Both maps show visible contrast between tissue types.

2.4   Fractional segmentation

The QUASAR post-processing software, written by Esben Petersen in Interactive Data Language (IDL), uses a binary segmentation based on the tissue relaxation rate (R_{1t}) histogram of the image series. By fitting three components to the histogram, appropriate thresholds can be chosen to segment the three compartments; cerebrospinal fluid (CSF), grey matter (GM) and white matter (WM). The segmentation can be used for calculation of means of quantities in different tissue

types, e.g., CBF in GM or aBV in WM. For convenience, the three compartments are also referred to as different "tissue types" henceforth (although, strictly speaking, CSF is not a tissue).

As a further development, we suggest the implementation of a modified version of a new fractional segmentation called "Fractional Signal mapping from Inversion Recovery" (FRASIER) (Shin et al., 2010). The FRASIER segmentation method uses inversion recovery of the longitudinal magnetization, i.e. the signal, which is registered with a Look-Locker sampling strategy. Since the read-out is similar to the one used in the QUASAR sequence (the most obvious difference being that FRASIER uses inversion recovery whereas QUASAR uses saturation recovery), the implementation was rather straight-forward and included some modifications and improvements. Among the improvements were that the correction of the flip angle could be exploited, which yielded maps of tissue-specific equilibrium (steady-state) magnetization $M_{ss,i}$ (see later in the chapter), instead of global values as in the original method. Furthermore, this exploitation also resulted in maps instead of global values of the effective longitudinal relaxation times $T_{1t,eff,i}$ which improved the segmentation.

It was assumed that the measured saturation recovery can be modelled as a linear combination of the different recovery functions of the three compartments, with limited interactions between them. The three monoexponential functions will then consist of different $M_{0,t,eff,i}$ and $T_{1t,eff,i}$ where i represents the type of contents, i.e., CSF, GM or WM. Figure 2.14 displays an example of these monoexponential functions in one voxel. The functions are estimations of the saturation recovery seen if the voxel had purely consisted of the respective tissue type. The segmentation basically consists of solving the linear combination of the individual tissue functions that build up the measured signal.
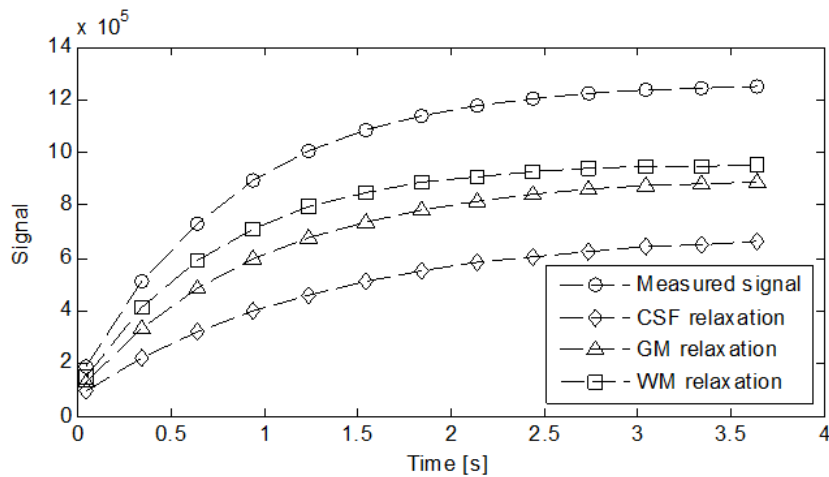

Figure 2.14: A measured saturation recovery (signal) and three available components with different relaxation times and limiting values. The segmentation problem consists of finding the linear combination of the three monoexponential recovery functions that best reproduces the measured signal.

For a saturation recovery, the measured signal can then be written as:

$$S(t) = \sum_i f_{s,i}\, M_{ss,i} \left(1 - A \cdot e^{-t/T_{1t,eff,i}}\right) \tag{2.19}$$

where $f_{s,i}$ is the fractional signal of tissue i (the fraction of the measured signal that can be assigned to tissue i), A is the fitting parameter from Eq. 2.16, $T_{1t,eff,i}$ is the effective relaxation times and

$$M_{ss,i} = \frac{1 - e^{-\frac{\Delta TI}{T_{1t,i}}}}{1 - \cos(\phi)\, e^{-\frac{\Delta TI}{T_{1t,i}}}} \tag{2.20}$$

where $T_{1t,i}$ is the true relaxation times for the different tissues, ϕ is the flip angle corrected for inhomogeneous excitation, and ΔTI is the time between the excitation pulses. $M_{ss,i}$ can be interpreted as the available magnetization if a voxel only contained the tissue type i. Comparing to Eq. 2.14 it is obvious that $f_{s,i}$ is the true $M_{0,t,i}$ and $M_{ss,i} = M_{0,t,eff,i}/M_{0,t,i}$. The chosen notation is, however, intuitive when speaking of fractional signals and more straightforward with regard to calculations. For a discrete set of N measured signal values $\mathbf{S_m} = [\,S(t_1)\,\dots\,S(t_N)]^T$, Eq. 2.19 can be written in matrix form as

$$\mathbf{S_m} = \mathbf{X}\mathbf{F_s} + \mathbf{e} \tag{2.21}$$

where

$$X_{i,j} = M_{ss,i}\left(1 - A \cdot e^{-t_j/T_{1t,eff,i}}\right), \;\; 1 \leq j \leq N \tag{2.22}$$

$$\mathbf{F_s} = \left[\, f_{s,CSF} \;\; f_{s,GM} \;\; f_{s,WM} \,\right]^T \tag{2.23}$$

and $\mathbf{e}$ is the column vector containing the measurement noise. With this formulation $\mathbf{F_s}$ can be estimated by means of linear least squares estimation, i.e., $\mathbf{F_s} = (\mathbf{X}^T\mathbf{X})^{-1}\mathbf{X}^T\mathbf{S_m}$, where $(\mathbf{X}^T\mathbf{X})^{-1}\mathbf{X}^T$ is the pseudo-inverse of $\mathbf{X}$.

To carry out the calculation, both the true and the effective relaxation times for the three different tissue types need to be determined (see Eqs. 2.19 and 2.20). An estimation of the true relaxation times for GM and WM can be obtained from the maximum values of a histogram over relaxation rates in the whole brain. The reason that relaxation rates is used instead of relaxation times is purely practical; the GM and WM components are easier to separate when studying the relaxation rates. An example of such a histogram is shown in Figure 2.15. The effective relaxation times can then be calculated voxel-by-voxel according to Eq. 2.15. The relaxation time of CSF is hard to estimate from the histogram since it has a wide spread and mixes excessively (in a given voxel), primarily with GM. Therefore the true relaxation time in CSF is assumed to be 3 s, and the effective relaxation time is calculated voxel-wise in the same manner as for GM and WM.
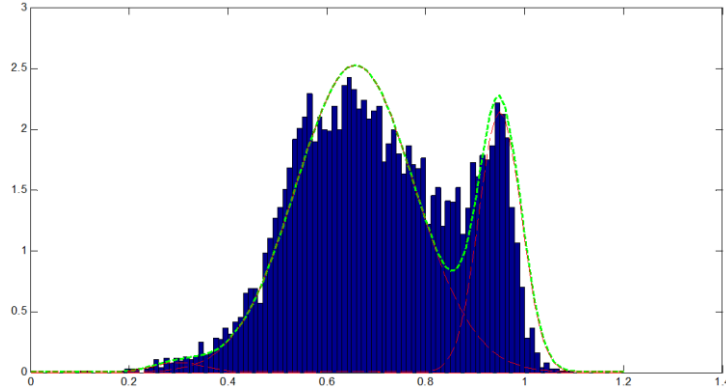
Figure 2.15: Relaxation times for GM and WM are estimated as the inverse of the two mean values of the relaxation rate histogram peaks. [s]

When the fractional signals have been obtained through the linear least squares estimation, the fractional volumes can be calculated by dividing by the water content of the tissue i:

$$f_{v,i} = \frac{f_{s,i}}{\rho_i} \qquad 2.24$$

Water contents of 100%, 89% and 73% were used for CSF, GM and WM, respectively (Donahue et al., 2006). Both the fractional signals and the fractional volumes can be constrained by $\sum_i f_{v/s,i} = 1$ to obtain normalized values.

Note that the method is based on T_1 mapping of the brain but does not exploit these maps per se (or the image contrast), but rather uses the unique magnetization recoveries of the different tissues, and is therefore dissimilar to other common MRI tissue segmentation methods.

2.5   Estimation of M$_{0,a}$

Different methods for estimating $M_{0,a}$, i.e. the magnetization available in fully relaxed arterial blood (at the current flip angle and field strength), have been used in the past. A common method is to use the signal from the sagittal sinus, assuming sufficiently good resolution to neglect any partial volume effect. Correction for the difference in T_2^* between arterial and venous blood can be applied. The drawback is that this method generally suffers from partial volume effects and high uncertainty since very few voxels can be used. An alternative approach is to calculate $M_{0,a}$ as the ratio between the equilibrium tissue magnetization $M_{0,t}$ and the brain blood partition coefficient λ (see Eq. 2.11). Petersen et al. compared three different methods for user-independent estimation of $M_{0,a}$ using this approach (Petersen 2009). In the first method, a global $M_{0,a}$ was calculated by dividing the mean $M_{0,t}$ in GM with a mean value of λ in GM. The exclusion of WM reflects the fact that WM CBF is difficult to measure by ASL due to low and delayed perfusion in WM leading to low signal-to-noise ratio (SNR). The measured signal (ΔM in Eq. 2.6) is

20

T_2^*-dependent and therefore $M_{0,a}$ should also reflect this T_2^* variation. The global value of $M_{0,a}$ will include average T_2^* effects in GM, but since these effects vary across the brain, errors could be introduced. The second method proposed is to divide $M_{0,t}$ with a λ which depends linearly on T_{1t}, given mean values for GM and WM. This assumes that the spin lattice relaxation is linear with proton density. The third method is to divide $M_{0,t}$ with an average full brain value for λ. Like the second method this also maps $M_{0,a}$ voxel-by-voxel and accounts for T_2^* effects, but it does not compensate for variations in λ. Petersen et al. pointed out that, if using method 3, it might be better to divide by the mean partition coefficient in GM since the CBF is only calculated for GM, and the use of a whole brain λ of 0.9 ml/g will systematically overestimate the CBF in GM. This variant of method 3 was therefore included in the present work and referred to as method 4. The methods can be summarized as:

$$\text{Method 1. } \overline{M_{0,a}} = \overline{M_{0,GM}} \, / \, \overline{\lambda_{GM}}$$

$$\text{Method 2. } M_{0,a} = M_{0,t} \, / \, \lambda_t(T_{1t})$$

$$\text{Method 3. } M_{0,a} = M_{0,t} \, / \, \overline{\lambda_{brain}}$$

$$\text{Method 4. } M_{0,a} = M_{0,t} \, / \, \overline{\lambda_{GM}}$$

where $\overline{e^{-TE/T_{2,GM}^*}}$ (the average T_2^* effects in GM) is included in $\overline{M_{0,GM}}$ (method 1) and e^{-TE/T_{2t}^*} (the T_2^* effects across the brain) is included in $M_{0,t}$ (methods 2 and 3). Petersen et al. found that their second method had the best performance (Petersen, 2009), which is intuitively reasonable since it respects both the variations of λ and T_2^* effects across the brain. In the QUASAR reproducibility study (Petersen et al., 2010) method 3 was used. Potentially improving on these methods, we propose a novel method for the estimation of $M_{0,a}$. This method uses the new implemented fractional segmentation to correct the equilibrium tissue magnetization for presence of CSF and to calculate a weighted value of the brain-blood partition coefficient.

Since arterial blood cannot normally be present in the CSF, its tissue-blood partition coefficient is zero. Previous methods do not consider this fact, which could introduce errors in the presence of partial volume effects, particularly with the low resolution of ASL. These errors would therefore be emphasized in voxels containing significant amounts of CSF, common in cortical grey matter (sulcal CSF) and periventricular tissues such as subcortical grey matter (ventricular CSF). The reason for this being frequently overlooked is probably that is has a rather small impact and perhaps due to a misinterpretation when applying the brain-blood partition coefficient in perfusion MRI. The brain-blood partition coefficient is often stated as the relation between proton densities in tissue and blood when used in ASL. This is an interpretation of the original definition of λ as the relation in distribution volumes between tissue and blood, for a water-based tracer. Following this original definition it becomes obvious that CSF should be excluded from the calculation, since a tissue only can be considered a part of the distribution volume provided that the tracer can distribute in that tissue. The proposed method is summarized mathematically below.

Assume that normalized fractional signals $f_{s,i}$ and volumes $f_{v,i}$ have been obtained through the modified FRASIER segmentation method explained earlier. An estimated value of λ can be calculated voxel-by-voxel as a weighted sum of the mean partition coefficients in GM and WM, where the weighting factors are the normalized fractional volumes of the respective tissues:

$$\lambda_{GM+WM} = f_{v,GM} \cdot \overline{\lambda_{GM}} + f_{v,WM} \cdot \overline{\lambda_{WM}}$$ 2.25

In this study, mean brain-blood partition coefficients of 0.98 ml/g and 0.82 ml/g were used for GM and WM, respectively. These mean values are based on PET measurements of the water content of blood, grey matter and white matter (Herscovitch and Raichle, 1985), and have been reproduced in ASL experiments (Roberts et al., 1996). As described above, the contribution from CSF should be excluded from the equilibrium tissue magnetization when calculating $M_{0,a} = M_{0,t}/\lambda$. This is done by removing the normalized fractional signal of CSF from $M_{0,t}$:

$$M_{0,GM+WM} = M_{0,t} \left(1 - f_{s,CSF}\right)$$ 2.26

Now, $M_{0,a}$ can be calculated in the traditional way:

$$M_{0,a} = \frac{M_{0,GM+WM}}{\lambda_{GM+WM}}$$ 2.27

where $e^{-TE/T_{2,GM+WM}^*}$ (the combined T_2^* effects of GM and WM) is included in $M_{0,GM+WM}$. As described earlier, $M_{0,a}$ should include T_2^* effects across the brain, requirement which could be violated with the suggested method since $M_{0,t}$ is altered. However, since T_2^* is long in CSF (compared with the parenchyma), the error is likely to be small for a TE of 23 ms. It should be noted that this new method cannot calculate $M_{0,a}$ in pure CSF, since λ is zero in these voxels. This problem can be bypassed by dividing the $M_{0,t}$ of such voxels with an average whole brain λ, but in reality this is irrelevant since CBF should be zero in these voxels anyway.

The presented approach is similar to method 2 described earlier, in which λ is calculated by linear relation to T_{1t}, although the new method employs no such assumption of linearity. The new method takes the definition of λ into account and could potentially improve ASL-based CBF quantification.

2.6   Deconvolution

Deconvolution is a problem that is common for many physiological systems when the quantity of interest is not directly measurable. Generally, the unknown quantity is either the system input or the system characteristics (the convolution kernel). Here we assume that the input is measurable and that the kernel is the unknown quantity. In such a case, the convolution kernel can be estimated by deconvolving the measured input with the measured noisy system output. The deconvolution problem is generally ill-posed, mainly meaning that there is no unique solution, and ill-conditioned, meaning that small errors in the measured data can induce large changes in the solution. When estimating the convolution kernel in physiological

systems more problems arise since the solution has to be realistic, e.g., smooth and/or positive.

Deconvolution problems can be solved by model-based (parametric) or model-free (non-parametric) methods. In the model-based methods the solution is modelled as a parametric function, avoiding the ill-posedness by reducing the problem into a parameter optimization. Model-based deconvolution will not be discussed to any extent in this paper. Model-free methods estimate the solution without any assumptions of the shape of the solution. One straightforward model-free deconvolution is the direct application of the convolution theorem. The convolution theorem states that a convolution in the time domain equals a multiplication in the frequency domain, and vice versa. Hence, by using the Fourier transform the unknown kernel can be estimated.

Another model-free approach is to use regularization as a way to stabilize the solution of the ill-posed inverse problem. Regularization uses a side constraint, supplementing the minimization of the sum of squares error between the reconvolved output (obtained by convolving the measured input with the estimated convolution kernel) and the measured noisy output data. The most common side constraint is that the solution should be smooth, which is realized by penalizing on the solution's derivates. Andrey Tychonoff was among the first to mathematically formalize this type of regularization, and this is why it is often referred to as Tikhonov regularization. The amount of smoothness is determined by the regularization parameter. A higher value on the regularization parameter yields a smoother solution, but at the cost of poorer correlation with the measured data. Figure 2.16 shows the basic idea of regularization.
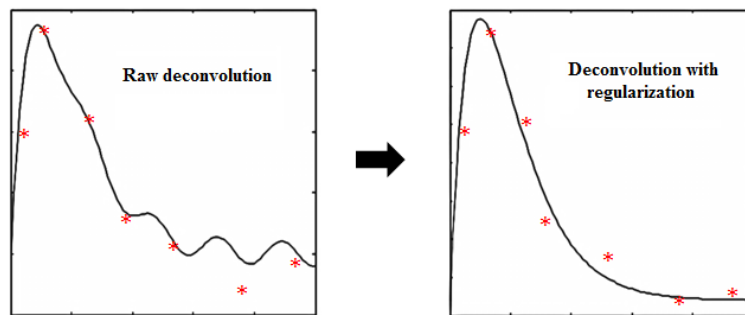

Figure 2.16: Arbitrary example of solution obtained by Tikhonov regularization (right) as compared to raw deconvolution (left). Red stars correspond to noisy measured output data and the solid line is the reconstructed output based on the estimated kernel. Instead of only optimizing on the residual errors, some deviation from the measured data is allowed as long as the solution has a certain degree of smoothness.

Regularization can be formulated mathematically by assuming a time-invariant linear system where $z(t)$ is the true output function, $g(t)$ is the input function and $u(t)$ is an unknown convolution kernel, together forming the convolution integral:

$$z(t) = \int_{-\infty}^{t} g(\tau) \cdot u(t - \tau) \, d\tau \qquad\qquad 2.28$$

similar to the convolution integrals discussed in previous sections. If $y(t) = z(t) + v(t)$ is the measured noisy output, where $v(t)$ is the noise affecting the measurements, the problem can be written in matrix form as $\mathbf{y} = \mathbf{Gu} + \mathbf{v}$, where $\mathbf{y}$ is a finite number of registered observations, $\mathbf{G}$ is the convolution with the input, $\mathbf{u}$ is the kernel and $\mathbf{v}$ is the measurement errors. The natural way to estimate the kernel is by direct inversion, $\hat{\mathbf{u}} = \mathbf{G}^{-1}\mathbf{y}$, which corresponds to minimizing the effects of noise and the difference between predicted and measured data, i.e. $\hat{\mathbf{u}} = argmin(\|\mathbf{y} - \mathbf{G}\hat{\mathbf{u}}\|^2)$. Regularization adds the side constraint to this minimization, and the regularized estimate of the input, given *a priori* information about the solution, can be written

$$\hat{\mathbf{u}} = argmin_{\hat{\mathbf{u}}}(\|\mathbf{y} - \mathbf{G}\hat{\mathbf{u}}\|^2 + \gamma^2 \|\mathbf{L}\hat{\mathbf{u}}\|^2) \qquad\qquad 2.29$$

where γ is the regularization parameter and $\mathbf{L}$ is the operator that introduces penalty if the solution does not follow the *a priori* expectation. As mentioned earlier $\mathbf{L}$ is often chosen as a derivative operator which bounds the solution to have a certain amount of smoothness. In that case the regularization parameter controls the amount of smoothness in relation to the residual error.

The deconvolution technique applied in this study, called non-linear stochastic regularization (NSR), is based on Tikhonov regularization, although interpreted in relation to the theory of statistical mathematics with the basic concepts remaining the same.

2.6.1 Deconvolution in perfusion MRI

A wide variety of deconvolution techniques have been used for MRI-based perfusion quantification in the past, mainly in contrast agent techniques such as DSC-MRI. For model-free deconvolution, Fourier transform (FT) is the most straightforward method. The method is insensitive to arterial delay but very sensitive to measurement noise. In practice, it is necessary to low-pass filter the transformed signals to remove high frequency components and thereby avoid overfitting. The result is highly dependent on how the user chooses to filter the transformed signals. Even if the signals are filtered consistently, Østergaard et al. showed that the result is biased, leading to underestimated CBF in the case of high blood flow rates (Østergaard et al., 1996). However, Wirestam et al. performed noise reduction of the measured data by wavelet transform followed by Fourier transform with a low regularization level and obtained satisfactory CBF values (Wirestam and Ståhlberg, 2005).

Gaussian process deconvolution is an alternative deconvolution method that employs a Gaussian process to generate smooth solutions by using a priori information (Andersen et al., 2002). However, the method does not account for the non-negativity of the residue function. Tikhonov regularization (described earlier) has also been used as an attempt to improve the physiological validity of the solved

residue function in DSC-MRI (Calamante et al., 2003). The method proved to reduce unwanted oscillations of the residue function, but it did not remove them completely and the non-negativity of the solution is not accounted for.

Block-circulant singular value decomposition (cSVD) is currently the most common deconvolution approach in perfusion MRI applications (Wu et al., 2003). This algorithm is a modified version of singular value decomposition (SVD), which formulates the deconvolution problem as an inverse matrix problem (Østergaard et al., 1996). By decomposing the input function into two orthogonal matrices and a non-negative diagonal matrix, the inverse of the input function matrix can be expressed as a matrix product. However, a threshold on the diagonal matrix is needed to avoid unphysiological oscillations (high frequency components) of the solution. The delay or time-shift sensitivity of SVD (the solution depends on the time of the measured signals rising edges) was solved by the introduction of cSVD, which uses zero-padding and edge-wrapping to compose a block-circulant input matrix. The use of cSVD benefits from low noise sensitivity and robust results. The drawbacks are that the same threshold as in SVD needs to be set by the user or by an automatic/adaptive algorithm, and that the solution generally does not follow the definition of the residue function, often violating the physiological characteristics such as monotonical decrease (non-oscillating) and non-negativity.

A great many other methods have been reported in the literature and each method has its own set of advantages and drawbacks. Zanderigo nicely reviews a great many deconvolution methods applied in DSC-MRI (Zanderigo, 2006).

2.7   Non-linear stochastic regularization

Regularization can be interpreted by means of stochastic mathematics if the unknown signals and parameters are described by probabilistics. De Nicolao et al. (de Nicolao et al., 1997) gives an excellent review of the regularization method for nonparametric input estimation, and at the same time proposing a stochastic formulation of the classical Tikhonov regularization, where the unknown signal is *a priori* modelled as the realization of a stochastic process (multiple integration of white Gaussian noise). The method provides statistically based criteria to compute the regularization parameter and other parameters such as the measurement noise if it is unknown. One problem with the method is that since the integrated random walk allows negative values, the solution is allowed to have negative values. This is often not desired in physiological functions and Pillonetto et al. suggested a new stochastic model that excluded negative values by modelling the unknown input as the exponential of a step-wise integration of white Gaussian noise (Pillonetto et al., 2002). Bell and Pillonetto built on these methods and solved the problem by placing a Bayesian prior on the function space and estimated unknown parameters by maximizing an approximation of the marginal likelihood where the unknown solution has been integrated out (Bell and Pillonetto, 2004). This allows a non-linear relationship between the unknown solution and the measured data. The estimated solution is calculated by maximizing the *a posteriori* probability density function

with the estimated parameters. This is all realized by constructing the solution as a linear combination of eigenvalues and eigenvectors, in theory allowing an infinite solution space. Furthermore, estimates of the solution rapidly converge to the true solution as the number of eigenvalues and eigenvectors increases, allowing the use of a low number and thereby reasonable calculation cost.

All three papers cited above emphasized the applicability to physiological measurements. Zanderigo et al. implemented the non-linear approach proposed by Bell et al., to solve the deconvolution problem in DSC-MRI (Zanderigo, 2006; Zanderigo et al., 2009). They called their method "Non-linear stochastic regularization" (NSR), and showed that it is capable of reproducing a realistic residue function better than most other commonly used deconvolution techniques, such as SVD or Tikhonov regularization (Zanderigo et al., 2009). A brief review of the theory behind NSR is given in the following paragraphs. The review is incomplete since the mathematical theory behind NSR is extensive and beyond the scope of a medical radiation physics MSc thesis. See (Bell and Pillonetto, 2004) and (Zanderigo, 2006) for the complete theory.

Non-linear stochastic regularization can be viewed as a Tikhonov regularization interpreted in a probabilistic manner. The residue function $R(t)$ is modelled as the realization of the integration over a stochastic process, given by Gaussian white noise. By using a non-linear Bayesian estimator and formulating a log-normal prior for the residue function, the deconvolution problem can be solved with the calculation steps proposed by Bell and Pillonetto (Bell and Pillonetto, 2004). Zanderigo et al. modelled $CBF \cdot R(t)$ as the convolution of the exponential of a Brownian motion (representing the integral of the Gaussian white noise), and an exponential function representing the arterial dispersion:

$$CBF \cdot R(t) = d(t) \otimes e^{R_1(t)} \qquad 2.30$$

where

$$d(t) = \frac{1}{\theta_1} e^{-t/\theta_1} \qquad 2.31$$

and

$$R_1(t) = a + \theta_2 \, \beta(t) \qquad 2.32$$

Here, $\beta(t)$ is the Brownian motion (stepwise integration of a white Gaussian noise), $d(t)$ is the modelled arterial dispersion, and θ_1, θ_2 and a are unkwon scalars. As mentioned earlier, the exponential ensures that the solution is non-negative.
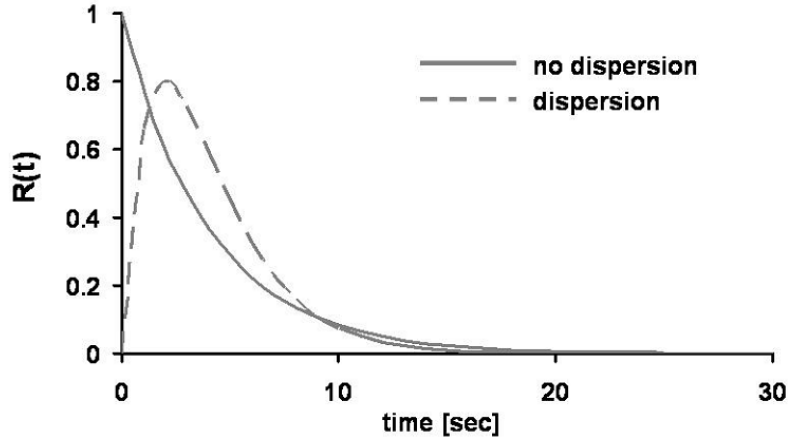
Figure 2.17: DSC-MRI residue function $R(t)$ with dispersion (dashed line) and corrected for dispersion (solid line). Image from Zanderigo 2006.

As mentioned in Chapter 2.1, the true AIF may be dispersed, compared to the measured one. This means that the arterial signal that we measure is not an exact AIF per definition, since that would demand the bolus to be registered exactly at the entrance of the local capillary system. In practice, the shape of the vascular bolus that is measured at a specific site might broaden on its way to the capillary system. By including the arterial dispersion in the model, it is possible to correct for potential errors due to the use of an incorrect AIF. In NSR, the dispersion $d(t)$ is modelled as a vascular transport function. This formulation was adopted from Calamante et al. (Calamante 2000), as a first approximation, assuming a well-mixed compartment. The formulation is easily derived since, given a well-mixed vasculature, the corresponding vascular residue function $R_{vasc}(t)$ can be expressed as an exponential, i.e., e^{-t/θ_1}, and the definition of the residue function (see Eq. 2.2) gives the vascular transport function as:

$$h_{vasc}(t) = -\frac{dR_{vasc}(t)}{dt} = \frac{1}{\theta_1}e^{-t/\theta_1} \qquad 2.33$$

This allows for the interpretation of θ_1 as a vascular mean transit time from the site of the measured AIF to the microvasculature, so that a larger θ_1 corresponds to more pronounced arterial dispersion. As θ_1 goes to zero, the dispersion function $d(t)$ approaches the delta function, corresponding to absent dispersion. It is important to point out that this is only a first approximation, since a particular vascular transport function will depend on many factors, such as the topology of the vasculature, the tissue type, the site of the measured AIF and the cerebral blood volume (CBV).

The inclusion of the vascular transport function allows the NSR algorithm to take dispersion of the bolus into account, by using the associative properties of convolution, i.e.:

$$[AIF(t) \otimes d(t)] \otimes R(t) = AIF(t) \otimes [d(t) \otimes R(t)] \qquad 2.34$$

where $AIF(t)$ is the measured AIF at a given site, $AIF(t) \otimes d(t)$ is the dispersed AIF at the entry of the microvasculature (i.e. the true AIF), and $d(t) \otimes R(t)$ can be seen as an effective (dispersed) residue function obtained due to the use of the non-dispersed AIF (CBF is left out for simplicity). This means not only that dispersion is incorporated in the model, but also that correction for dispersion can be made by reproducing the undispersed $CBF \cdot R(t)$. This is a huge advantage compared to many other deconvolution techniques since dispersion can cause significant underestimation of the CBF. Figure 2.17 shows an example of a residue function deformed due to arterial dispersion (dashed line) and the same residue function corrected for dispersion (solid line). Another advantage of NSR is that it reproduces the residue function on a fine virtual time grid which yields smooth results with an apparently high temporal resolution. It should be noted that the resolution of the virtual grid needs to be determined by the user and that the AIF must have the same temporal resolution which, in this work, was solved by exploiting the gamma-variate fit of each AIF. In this work a virtual temporal resolution of 25 ms was chosen, compared to the real temporal resolution of 300 ms for the measured data. Note that in the present work it is the broadening of the AIF from the site of the measurement to the site of the capillary system that is referred to as arterial dispersion, and not from the labelling site to the measurement site.

It is important to emphasize that NSR is not a parametric model in the deterministic sense even if, in a way, $CBF \cdot R(t)$ is modelled. The prior for $R(t)$ is namely specified over an infinite dimensional function space. This means that the prior model describes a very general shape, allowing a wide variety of different residue functions, not restricted as for a parametric function.

In order to formulate the NSR optimization in matrix form (in the same manner as Eq. 2.29), we assume that $\mathbf{y}$ is the measured tissue signal, $\mathbf{G}$ is the convolution with the AIF, $\boldsymbol{\Sigma_v}$ is the covariance matrix containing the measurement noise, including an unknown scalar θ_3, and $\mathbf{R_1}$ is the residue function to be estimated. Then, after the unknown scalars θ_1, θ_2, θ_3, a and γ (the regularization parameter; see below) have been determined through the optimization of an approximation of the marginal likelihood, the maximum *a posteriori* estimate of $\mathbf{R_1}$ is given by:

$$\widehat{\mathbf{R}}_1 = \arg\min_{\mathbf{R_1}} \left[(\mathbf{y} - \mathbf{G}[\mathbf{d} \otimes e^{\mathbf{R_1}}])^T \, \boldsymbol{\Sigma}_v^{-1} \, (\mathbf{y} - \mathbf{G}[\mathbf{d} \otimes e^{\mathbf{R_1}}]) + \gamma^{-2} \int (\dot{\mathbf{R}}_1)^2 dt \right] \quad 2.35$$

where $\dot{\mathbf{R}}_1$ is the time derivate of $\mathbf{R_1}$ and γ is the regularization parameter controlling the smoothness of the solution. Note that the regularization parameter is not chosen by the user, but set automatically in the preceding parameter estimation.

2.7.1   ASL-NSR Implementation
To apply NSR to time-resolved ASL data, some modifications were necessary. Firstly, the measurement noise is modelled as $\theta_3 / (1 + y)$ by Zanderigo et al. (Zanderigo, 2006). With the low SNR in ASL experiments, the same model cannot be used (see Figure 2.18). However, ASL enables an estimation of the measurement error, since it is based on repeated experiments. The calculated population standard

deviation of ΔM, calculated on a voxel-by-voxel basis and for every time point, makes a good starting value for the measurement noise when optimizing the unknown scalars (where θ_3 is the one related to the noise amplitude). Hence, the measurement noise in our implementation is modelled as $\theta_3 \cdot SD_{\Delta M}$, where $SD_{\Delta M}$ is the standard deviation of the repeated measurements of ΔM.
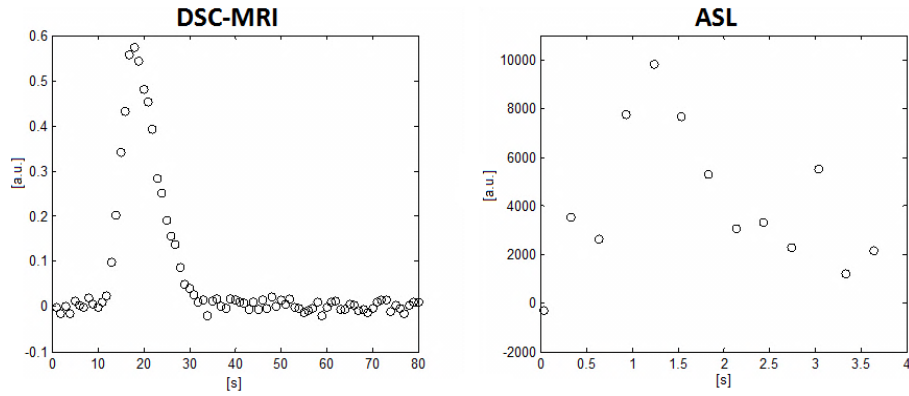

Figure 2.18: Comparison of the measurement noise in two different bolus-tracking experiments; DSC-MRI and ASL. The figures display measured signal in arbitrary units as a function of time in seconds. The relative amplitude of the measurement noise is significantly higher for the ASL data.
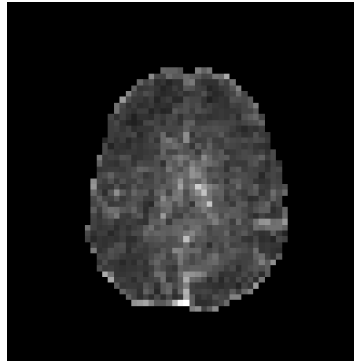

Figure 2.19: Example map of the estimation of the measurement error, calculated as the standard deviation of the repeated measurements.

The delay sensitivity of deconvolution methods employing stochastic approaches has to our knowledge not been thoroughly reviewed. Note that the delay discussed in this study is the time it takes for the arterial bolus to travel from the actual AIF measurement site to the entrance of the capillary system, i.e., not the arterial delay (from labelling site to capillary system) generally referred to in ASL experiments. An artificial tissue signal and arterial input function was used to get an indication of

the delay sensitivity of NSR. The tissue signal was shifted in small increments, forcing it to start before the start of the AIF (simulating inappropriate AIF selection at a site where the bolus is delayed compared with the tissue site) as well as after the input function (simulating conventional arterial delay). From this study, it was concluded that the NSR algorithm is rather sensitive to delay (see Chapter 4.6). Therefore, a shift of the AIF was implemented. The size of the shift was chosen so that the start of the AIF, as well as possible, coincided with the start of the tissue signal. This was motivated by the fact that the beginning of the true AIF should coincide with the first labelled water molecule passing the entrance to the capillary system, and so should the start of the tissue signal (which consists of the combined signal from labelled spins in the microvascular system and the exchanged labelled spins in the tissue). Thus, by incorporating this correction for arterial delay, as well as the correction for arterial dispersion, the resulting AIF should be closer to the true AIF.

As mentioned earlier, the residue function is a monotonically decreasing function per definition. There is, however, no such constraint on the solution (corrected for dispersion) in NSR, in principle allowing $R(t)$ to show any shape, including shapes without monotonical decrease. In some cases, this poses a problem when using ASL data since an inappropriately selected or significantly delayed AIF, as well as a noisy tissue signal, can lead the algorithm to a solution that is not monotonically decreasing. These inaccurate solutions can be avoided by introducing a measure of the degree of monotonical decrease for the solution. If the solution is a discrete vector $\mathbf{R} = [R_1, \ R_2, \ \dots, R_N]$, the first forward difference of this vector is:

$$\mathbf{\Delta R} = [R_2 - R_1, \ R_3 - R_2, \dots, \ R_N - R_{N-1}] \qquad 2.36$$

All elements of this difference vector should be non-positive for the solution to be considered non-increasing. The parameter

$$\delta_{inc} = \sum_i \Delta R_i^* \qquad 2.37$$

where

$$\Delta R_i^* = \begin{cases} \Delta R_i, & \Delta R_i > 0 \\ 0, & \Delta R_i \leq 0 \end{cases} \qquad 2.38$$

is the sum of all positive values of the difference vector, works as a measure of the increasing behavior of the solution. Now, any increase of the solution can be minimized by incorporating this parameter as a second side-constraint in the optimization process of NSR. If the solution follows the definition, then δ_{inc} is zero and the optimization procedure works as usual (i.e., optimizes on the square deviations and the smoothness of the solution), but if the solution is not monotonically decreasing, the optimization process includes the minimization of δ_{inc}.

3 Materials and methods

3.1 Subjects and imaging protocol

Data from ten volunteers (6 male, 4 female, age 21-65) investigated within the QUASAR test-retest study (Petersen et al., 2010) were used in this study. The experiments were performed with a Philips Achieva 3T MRI unit (Philips Medical Systems, Best, The Netherlands) using an 8-element head coil. The pulse sequence used the following protocol: 7 slices, 6 mm slice-thickness, 2 mm slice gap, 64×64 matrix, 240×240 mm^2 FOV, 35°/11.7° flip angles, TR/TE/ΔTI/TI$_1$ = 4000/23/300/40 ms, 13 inversion times, 84 series (48 crushed, 24 non-crushed and 12 low flip angle - alternating label and control), 2.5 SENSE factor, 150 mm labelling thickness, 3.75×3.75 mm^2 in-plane resolution and a total scantime of 6 min. Raw data were exported in Philips PAR/REC file format.

3.2 Post-processing

Raw QUASAR data were exported to a PC running MATLAB 2010b (The MathWorks, Inc., Natick, MA, USA). The data were post-processed using an in-house software built on the model-free ASL method as proposed by Petersen et al. (Petersen, 2009; Petersen et al., 2006a), and NSR software written by Zanderigo et al., available at http://www.dei.unipd.it/ricerca/bioing/nsr_software (Zanderigo et al., 2009). Data were also post-processed with the QUASAR software written by Petersen to obtain CBF maps corresponding to deconvolution with cSVD.

Each session consisted of 7644 2D images. Magnitude images were sorted into slices, time points, label/control and the three different sequence types (crushed, non-crushed and low flip angle). A whole-brain mask was automatically generated by using an adaptive threshold combined with minor erosion and dilation, to avoid unnecessary calculations in irrelevant voxels. Effective equilibrium magnetization of tissue, $M_{0,t,eff}$, and effective longitudinal relaxation time of tissue, $T_{1t,eff}$, were mapped in the whole brain by fitting an ideal saturation recovery to the measured non-crushed data, as described in section 2.3.3. $T_{1t,eff}$ was also mapped for the low flip angle acquisitions to enable estimation of the flip angle correction (see section 2.3.4). Longitudinal relaxation time of tissue, T_{1t}, and equilibrium magnetization of tissue, $M_{0,t}$, were calculated through Eqs. 2.14 and 2.15.

The whole brain was segmented into fractional maps of GM, WM and CSF by using non-crushed data, calculated relaxation times of tissue, calculated equilibrium magnetization of tissue and true flip angles as parameters in the modified FRASIER segmentation described in section 2.4. Resulting fractional volumes and signals were used to calculate $M_{0,a}$ by the novel method described in section 2.5. For comparison, $M_{0,a}$ was also estimated using the four previously proposed methods, all described in section 2.5.

Perfusion-weighted images, ΔM, were obtained by subtracting labelled images from control images using the crushed data. ΔM images with large deviations from the mean image were assumed artifactual and therefore omitted from the study.

A dynamic vascular signal was obtained for every voxel by subtracting crushed data from non-crushed data. A gamma-variate of the form $A \cdot (t - t_0)^B \cdot e^{-t/C}$, where A, B, C and t_0 are fitting parameters, was fitted to the vascular signal. Arterial blood volume (aBV) was calculated by dividing the area under the gamma-variate function accounted for relaxation of arterial blood, assuming a T_{1a} of 1.65 s (Lu et al., 2004), with the area of the theoretical labelling bolus, i.e., $2 \cdot M_{0,a} \cdot \tau_b \cdot \alpha$, where τ_b is the bolus length (640 ms) as predefined through the bolus saturations incorporated into the sequence and α is the labelling efficiency assumed to be 0.95. The arterial signal is only reasonably high in a limited number of voxels in the brain and voxels with an aBV exceeding 1.2% were identified as potential AIFs. However, AIFs with a poor gamma-variate fit were considered too noisy and were omitted. Figure 3.1**Fel! Hittar inte referenskälla.** displays an example of accepted AIFs in a single brain slice. Since each tissue signal is to be deconvolved with an AIF, the Euclidian distance in three dimensions was used to identify the closest AIF for every voxel in the brain. An automatic edge detection using the classical Canny algorithm was used to identify the time of the start of both the AIF (τ_a) and the non-crushed perfusion weighted tissue signal (τ_m). Based on the AIF that was selected through the Euclidian distance condition, the AIF of each voxel exhibited a unique set of parameters, i.e., the vascular-microvascular transit time ($\tau_m - \tau_a$; correction for relaxation of the labelled spins), the number of excitation pulses during that transit time (correction factor $\cos^n \phi$; see section 2.3.1 for details) and the equilibrium magnetization of arterial blood at the site of the tissue voxel ($M_{0,a}$; scales the AIF to the full magnetization difference). All AIFs were subsequently shifted in time to minimize the time between the start of the AIF and the tissue curve.
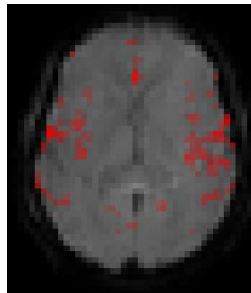

Figure 3.1: Example of selected AIFs. The intensity of the red color corresponds to the aBV of each AIF.

Deconvolution was performed using NSR applied to the corresponding AIF and tissue signals for one voxel at a time (see section 2.7 for details on NSR). The deconvolution technique was modified as described in section 2.7.1 to be applicable to the QUASAR data. The NSR algorithm demands a predefined number of

eigenvalues and eigenvectors, N, which was fixed to 10 throughout the study. The virtual time grid had an increment of 25 ms and spanned from 25 ms to 4 s. Starting values for the optimization process was $\theta_1=0.1$, $\theta_2=1$ and $\theta_3=0.2$. The standard deviation of ΔM was used as the estimated measurement error in the NSR optimization. The proposed extra side-constraint (see section 2.7.1) was reviewed but only preliminary results are presented, and the side-constraint was not used in the other results of this study. Deconvolution was also carried out with cSVD in a limited number of cases to compare the visual cSVD characteristics of kinetic curves with those of NSR. Software written by and received from Petersen was used for comparison of absolute CBF values as calculated with cSVD.

3.3   Analysis

Results from the NSR deconvolution, NSR with correction for dispersion (NSR$_{CD}$) and cSVD were visually evaluated by displaying CBF maps, as well as kinetic curves of AIF, tissue signal and solved residue function. Reconvolved tissue signals were obtained and superimposed on the measured tissue signal by convolving the solved residue function with the corresponding AIF. The effect of the dispersion correction was quantified by comparing calculated CBF values with NSR and NSR$_{CD}$ both in whole brain and in GM. Voxels were defined to be GM if they had a fractional volume of GM, as obtained from the segmentation, higher than 80%.

The fractional segmentation was visually evaluated by displaying probability maps of the different tissue types as well as combined maps in which each tissue type corresponded to a specific color. The novel method for estimating $M_{0,a}$ was compared with the four previous methods, both visually and using absolute and relative values in the whole brain as well as in GM only (fractional volume threshold of 80%). A statistical t-test (two-sample paired difference, 5% significance level) was used to see if the novel method differed significantly from any of the two most realistic methods (method 2 and method 4).

The delay sensitivity of NSR was investigated by using simulated DSC-MRI data and shifting the AIF in small increments. The result was evaluated by studying the maximum value (in arbitrary units) of the residue function as a function of the time shift, as well as by observing how the residue function characteristic changed with the amount of shift.

4 Results

4.1 Fractional segmentation

The implementation of a fractional segmentation was quite successful. The calculation of pure tissue voxel magnetizations (Eq. 2.20) yielded maps of this parameter for the different tissue types, as seen in Figure 4.1. The different tissue types have different mean values corresponding to different equilibrium magnetizations. The maps are not homogenous due to the imperfect excitation RF pulses (cf. Figure 2.12). Figure 4.2 shows an example of the resulting normalized fractional signals in a slice in one subject, and Figure 4.3 shows the same for normalized fractional volumes. The two latter figures are similar to each other since the only difference is the inclusion of tissue water densities in the fractional volumes.
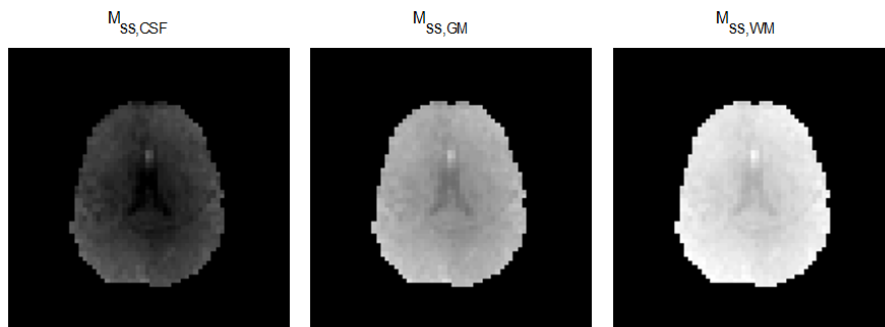
Figure 4.1: Available magnetization for pure tissue voxels. From left to right: CSF, GM and WM. The maps have the same grey scale.
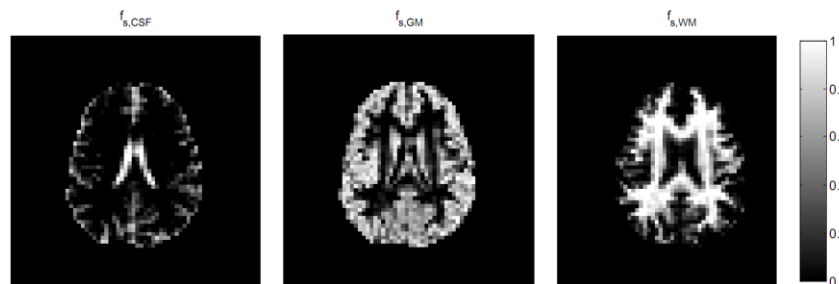

Figure 4.2: Fractional signals for CSF, GM and WM (left to right), normalized to show values between zero and one.
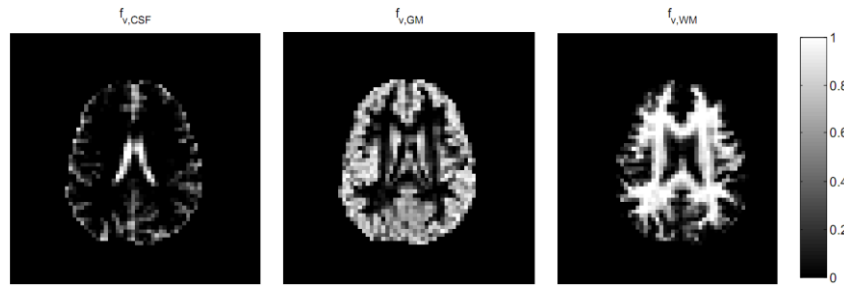
Figure 4.3: Fractional volumes for CSF, GM and WM (left to right), normalized to show values between zero and one.

The segmentation in one slice can be viewed in a single image by allocating separate colours to different tissues. In Figure 4.4, this procedure has been used to display the fractional volumes of all slices in one subject.
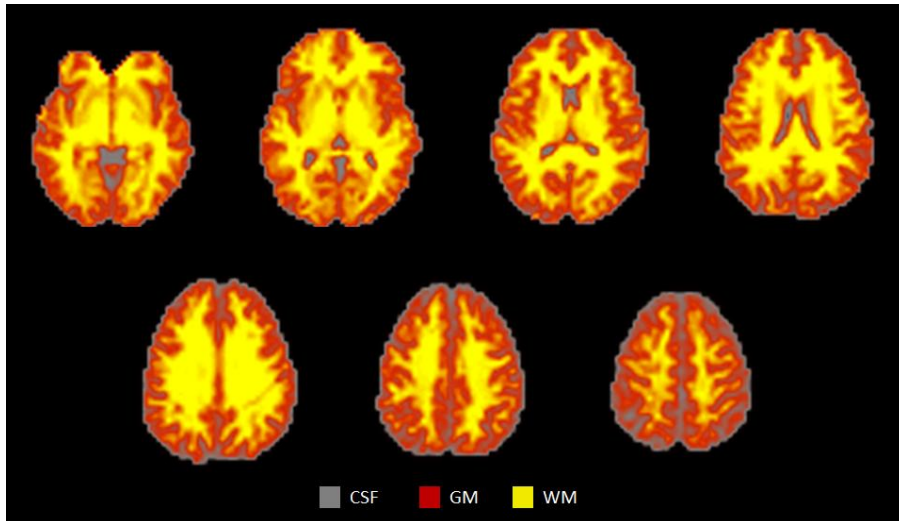

Figure 4.4: Fractional segmentation maps of seven slices in a subject. The images are cubically interpolated to enhance the visualization.

4.2   Estimation of M$_{0,a}$

The novel method for estimation of $M_{0,a}$ was feasible. It resulted in similar absolute values of $M_{0,a}$ as those calculated by previously proposed methods (Petersen, 2009). However, the novel method resulted in generally more homogeneous maps of $M_{0,a}$. Figure 4.5 shows an example of $M_{0,GM+WM}$, λ_{GM+WM} and the resulting map of $M_{0,a}$ obtained by dividing the former two.
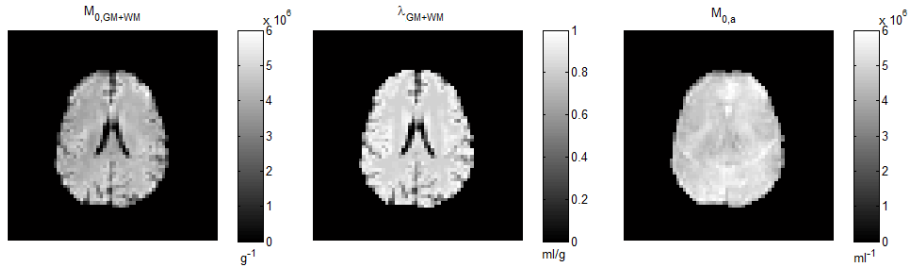
Figure 4.5: From left to right: Tissue equilibrium magnetization without signal originating from CSF ($M_{0,GM+WM}$), estimated map of the brain-blood partition coefficient (λ_{GM+WM}), and the estimated equilibrium magnetization in arterial blood ($M_{0,a} = M_{0,GM+WM}/\lambda_{GM+WM}$).

The novel method is visually compared to the previously three proposed methods, as well as a fourth method called "method 4" which is the same as "method 3" but using a mean whole brain λ of 0.98 ml/g instead of 0.90 ml/g (i.e., the literature value for GM instead of for whole brain). Figure 4.6 shows $M_{0,t}$, λ and $M_{0,a}$ for the different methods (method 1-4 and the novel method) in one slice in one subject. $M_{0,a}$ for all five methods is shown for all slices in one subject in Figure 4.7.
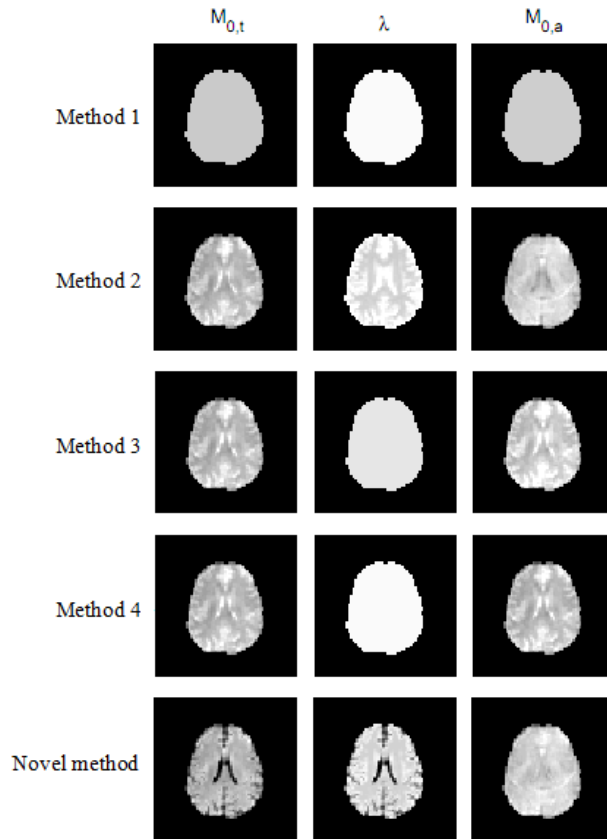

Figure 4.6: $M_{0,t}$, λ and $M_{0,a}$ for the different methods. From top to bottom: Method 1-4, and the novel method.
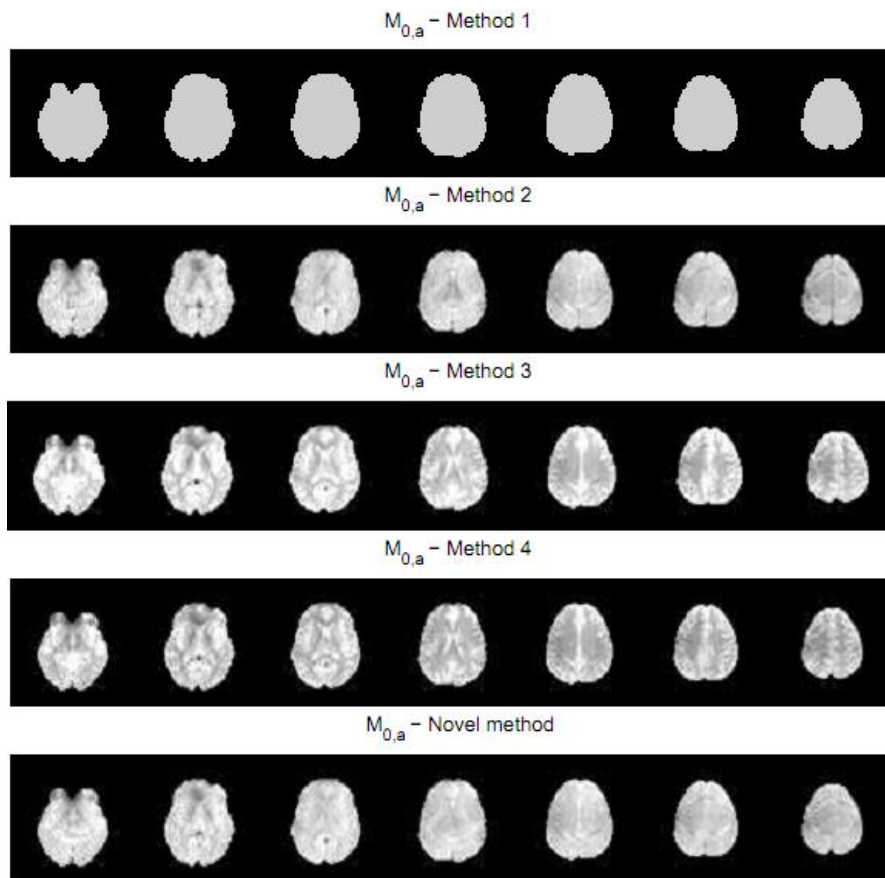
Figure 4.7: $M_{0,a}$ in all slices in one subject for the different methods. Slices are in inferior-superior from left to right.

In Figure 4.8 the mean value of $M_{0,a}$ in the whole brain is compared to the mean values of $M_{0,a}$ as obtained with the other four methods. A value larger than one corresponds to a higher mean $M_{0,a}$ with the novel method, and a value lower than one corresponds to a higher mean $M_{0,a}$ for the alternative method. Remember that the value of $M_{0,a}$ scales the CBF linearly. Figure 4.9 shows the same but only for voxels considered to be GM. In general, the novel method results in slightly higher mean values on $M_{0,a}$. However, as expected, method 3 results in higher $M_{0,a}$ than any other method, since it underestimates λ, at least in GM voxels. Furthermore, in Figure 4.9, methods 1 and 4 coincide. This is obvious since both methods use a mean brain-blood partition coefficient of 0.98 ml/g, and looking at GM only, both method also use $\overline{M_{0,GM}}$ in the calculation of the mean of $M_{0,a}$.
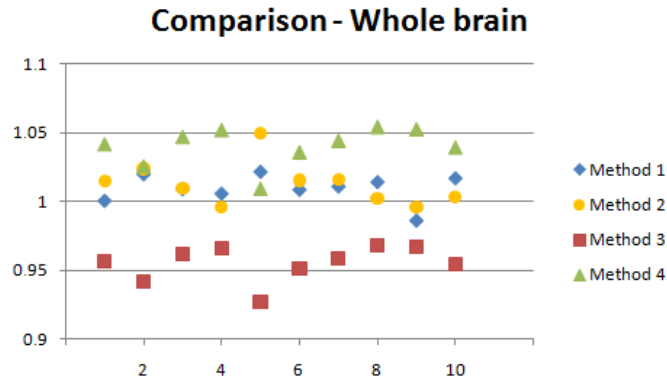
Figure 4.8: Mean $M_{0,a}$ of the whole brain with the novel method, divided by the means obtained by methods 1-4. Subject 1-10 on the x-axis.
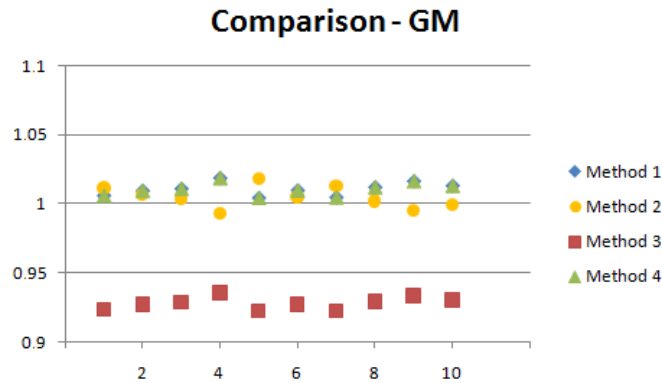

Figure 4.9: Mean $M_{0,a}$ in GM with the novel method, divided by the means obtained by methods 1-4. Subject 1-10 on the x-axis.

The novel method was also compared to the other methods in terms of absolute values. Figure 4.10 displays absolute mean $M_{0,a}$ in GM for the different methods. The mean value of $M_{0,a}$ in GM was consistently higher with the novel method as compared to method 4 (p<0.001, two-sided t-test), but not compared to method 2 (p>0.05, two-sided t-test). Once again the overestimation of $M_{0,a}$ with method 3, due to the underestimation of the brain-blood partition coefficient in GM, is clear. Disregarding method 3, which clearly overestimates $M_{0,a}$ in GM, all methods generated quite similar mean $M_{0,a}$ in GM.
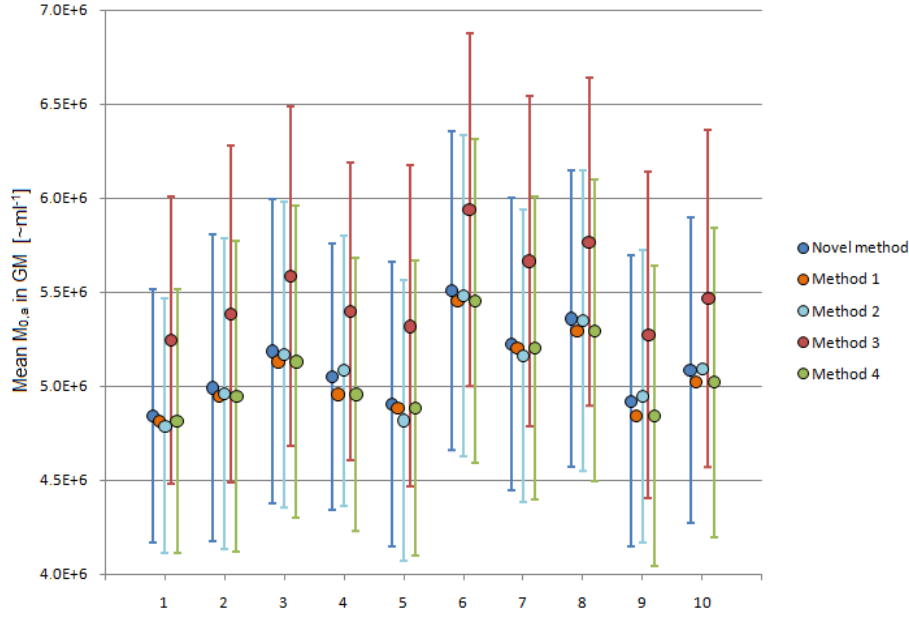
Figure 4.10: Absolute mean values of $M_{0,a}$ in GM voxels for the novel method (blue), method 1 (orange), method 2 (light blue), method 3 (red) and method 4 (green) for the ten subjects. The error bars correspond to one standard deviation.

4.3 Residue function characteristics

It is difficult to quantify CBF in WM using ASL, since WM has lower perfusion signal and longer bolus arrival times. Hence, this work is primarily concerned with the quantification in GM. Figure 4.11 displays an example of dynamic functions, and the resulting residue function, for one GM voxel. The AIF corresponds to the fitted gamma-variate on the virtual time grid. In the middle figure, circles represent the measured $\Delta M(t)$ and the solid line is the reconvolved tissue signal, which is obtained by convolving the solved residue function (from the deconvolution) with the fitted AIF. The square sum of the deviations between the measured data and the reconvolved function is the actual residual norm which is part of the minimization optimization process of the deconvolution. The figure to the right displays the solved residue function, with (solid line) and without (dotted line) correction for dispersion. Comparing to Eq. 2.30 the solid line corresponds to $e^{R_1(t)}$ and the dotted line corresponds to $d(t) \otimes e^{R_1(t)}$. It is clear that the corrected residue function follows the definitions of monotonical decrease and non-negativity.

The example in Figure 4.11 is representative in that the experiment is slightly too short for the tissue signal to return to baseline, which results in both a reconvolved tissue signal and a residue function that do not converge to zero. On the other hand, the example does not represent all cases since not all GM voxels resulted in a corrected residue function that was monotonically decreasing (all residue functions followed the non-negativity according to the nature of NSR).
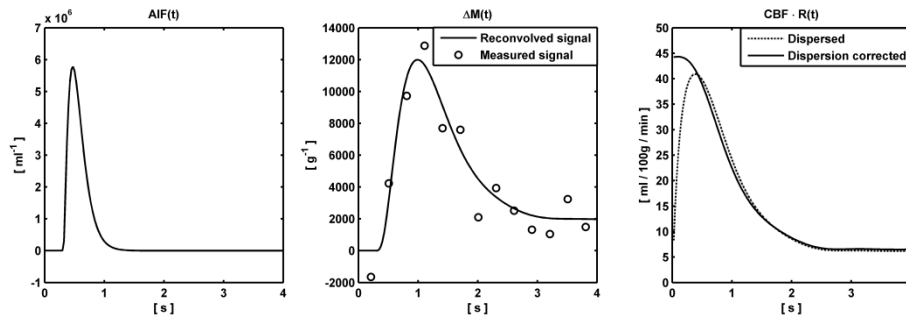
Figure 4.11: *Left:* The gamma-variate fitted AIF, normalized for the current voxel. *Middle:* The measured $\Delta M(t)$ data (circles) and the reconvolved tissue signal (solid line). *Right:* The residue function obtained by deconvolution with NSR, with (solid line) and without (dotted line) correction for arterial dispersion.

Since each session resulted in several thousand tissue voxels and every tissue voxel has a unique solved residue function, it is difficult to display a general residue function. Therefore, a few examples of some different representative residue functions obtained with the implementation are shown in Figure 4.12. Figure 4.12a shows a common result which can be interpreted as very little arterial dispersion, since the two curves are almost identical. The shape of the residue function is definitely realistic, since it follows an approximately exponential decrease as expected from the relaxation of labelled spins. Figure 4.12b displays an extreme amount of arterial dispersion. This is a good example of the potential errors in quantified CBF if correction for arterial dispersion is disregarded. Figure 4.12c displays a pretty common result with a moderate arterial dispersion and a noticeable "hump" around the middle of the curve. The hump is the result of a small increase in the tissue signal about 1-2 s after the signal peak. Figure 4.12d shows a common and satisfactory result with a moderate arterial dispersion and a monotonically decreasing corrected residue function. The figure also displays a very common characteristic in that the residue function does not converge to zero since the tissue signal has not returned to baseline during the course of the experiment. Figure 4.12e shows a result which corresponds to a failed optimization in the deconvolution process. This could for example be due to an excessively noisy tissue signal, extreme delay or bad starting values for the optimization parameters. Figure 4.12f is similar to Figure 4.12c although the hump is larger which results in an unrealistically oscillating residue function. Note that the proposed modification that could potentially avoid these kinds of errors (see section 2.7.1 and 5.7) has not yet been implemented due to the lack of a proper validation of its reliability.
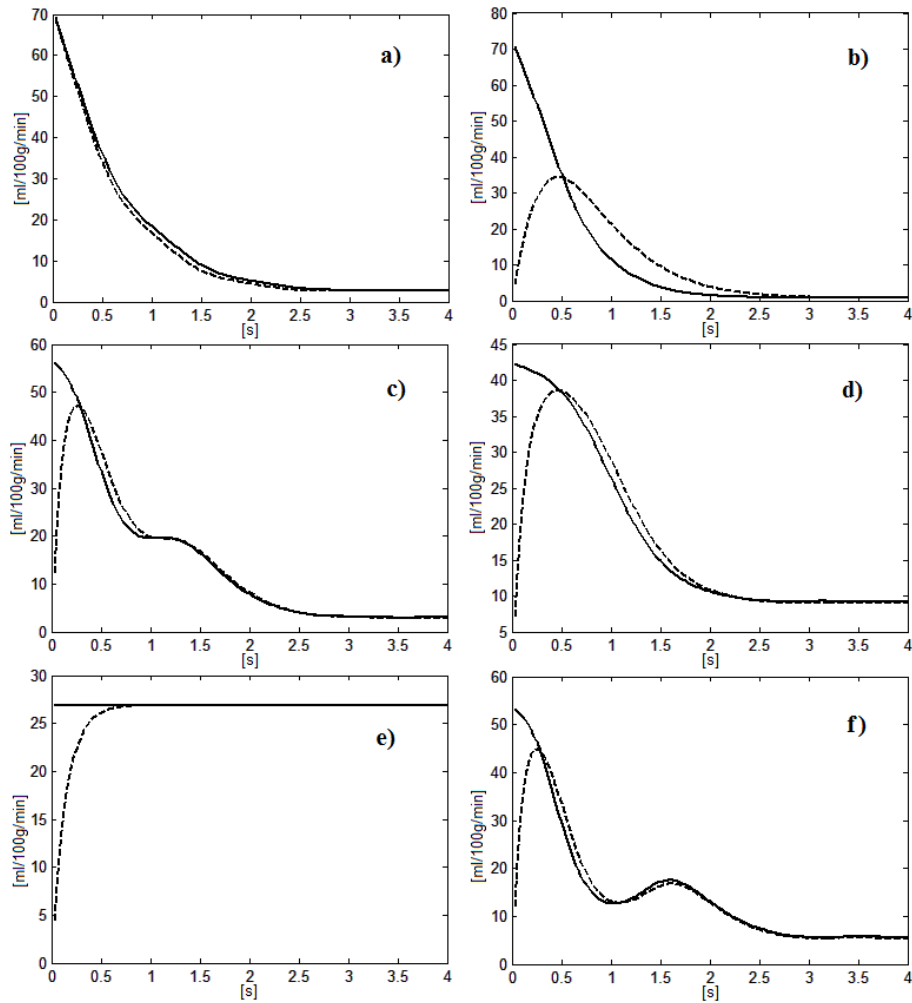
Figure 4.12: Examples of different solved residue functions for different GM voxels. All six figures have $CBF \cdot R(t)$ on the y-axis and time on the x-axis. Solid line corresponds to a residue function corrected for arterial dispersion and dashed line is the corresponding uncorrected residue function. a)-d) are results which are regarded to be satisfactory and e)-f) are examples of results that are physiologically unrealistic.

The appearance of the resolved residue function depends on the eigenvalues that the optimization calculates, together with the three NSR parameters θ_1, θ_2 and θ_3. As described in more detail in the theory chapter, θ_1 is the estimation of the amount of arterial dispersion, θ_2 is connected to the non dispersed and non negative residue function and θ_3 is the estimated noise level, or more precise, the fraction of the noise level stated by the user that the optimization recognizes. Figure 4.13 displays examples of these parameters in one slice and subject.
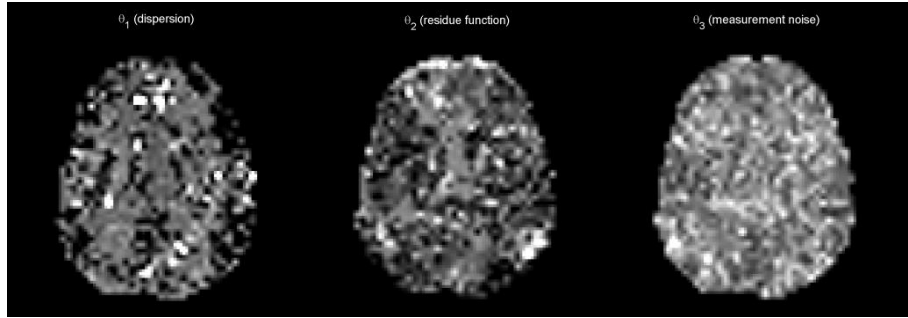
Figure 4.13: From left to right: Example of parameter maps of θ_1, θ_2 and θ_3.

Comparing to cSVD, which is probably the most common deconvolution technique in perfusion MRI and also the one used in previous QUASAR implementations (Petersen et al., 2006a; Petersen et al., 2010), it is clear that NSR consistently produced much more realistic residue curves, without any need for thresholds or oscillation indexing to suppress oscillations. Figure 4.14 displays the AIF, the tissue signal (measured and reconvolved) and the estimated residue function in a typical GM voxel, obtained by both NSR and cSVD. Even though a threshold was used to suppress the oscillations in cSVD, the result violates the definition of the residue function. Furthermore, NSR respects measurement errors in a more natural way, rendering a smooth residue function and consequently smooth realistic reconvolved tissue curves.
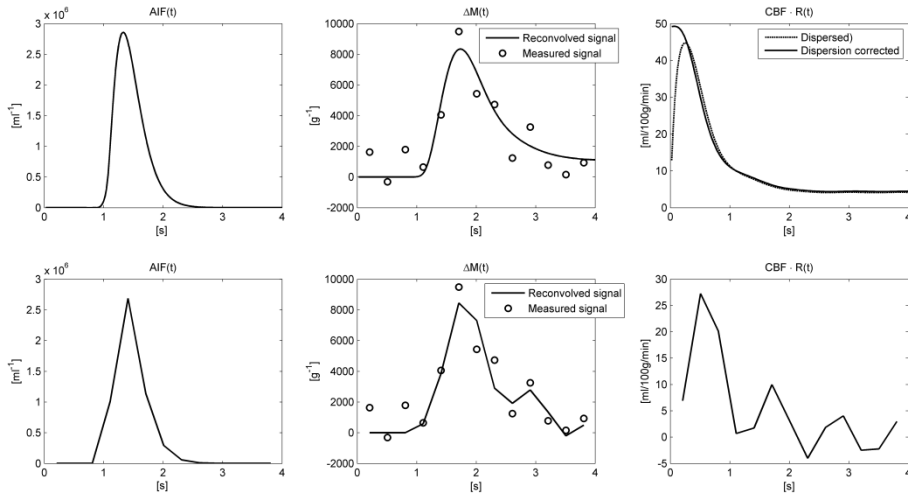

Figure 4.14: A typical deconvolution case, solved with NSR (top) and cSVD (bottom). Left column is the fitted AIF (cSVD has the experimental temporal resolution), middle column is measured and reconvolved tissue signal and right shows the solved residue function. Note the negative values and oscillating behavior of the residue function solved by cSVD.

4.4 Arterial dispersion correction

It is visually clear from the displayed solved residue functions that the dispersion correction (as a part of NSR) has some effect on the quantitative CBF. Table 4.1 summarizes a study of the effect of the arterial dispersion correction on the absolute CBF in GM. It displays different measures of the effect for the ten subjects individually and in mean. The first table row shows the amount of GM voxels (in percent of all GM voxels) that show a dispersion correction effect larger than 5% on the CBF value. The mean value implies that 30% of the GM voxels has a dispersion correction effect larger than 5%. The next row is the same calculation but shows the amount of voxels that has a correction effect on CBF which is below 1%. This limit is regarded to correspond to negligible correction effect. This means that in average, 46% of the GM voxels has no dispersion correction effect and 54% has a non-negligible effect. The third row corresponds to the amount of voxels that has a correction effect larger than 5%, in percent of the voxels that show a non-negligible effect. For example, for subject 1 this means that 55% of the GM voxels has a non-negligible correction effect, and out of these, 57% has a correction effect larger than 5%. The fourth row is the actual dispersion correction effect on the absolute CBF in all GM voxels, and the last row is the same but omitting the voxels with a negligible effect. The mean CBF correction effect for all GM voxels in all subjects is 6%, and when omitting voxels with negligible effect it is 10%.

Table 4.1: Dispersion correction effect on calculated CBF for the ten subjects. All measures are stated in percent.

Subject:	1	2	3	4	5	6	7	8	9	10	Mean
Percent of GM voxels over 5% effect:	31	34	28	17	34	34	30	28	28	31	30
Percent of GM voxels below 1% effect:	45	36	46	61	42	41	44	53	49	44	46
Percent of GM voxels (with non-neglible effect) over 5% effect:	57	53	52	44	59	58	54	59	54	56	55
Effect for GM voxels (Mean±SD):	6±13	7±12	5±9	3±7	6±11	7±14	6±12	5±13	5±13	6±11	6±12
Effect for GM voxels (with non-neglible effect) over 1% (Mean±SD):	10±16	10±14	9±10	8±10	10±13	11±16	10±14	11±17	10±16	10±14	10±14

The mean correction effect has a standard deviation that overlaps zero. There are indeed a few voxels that actually display a negative correction effect, but mainly it depends on the distribution of the correction effect. Figure 4.15 shows an example of a histogram over the correction effect in one subject.
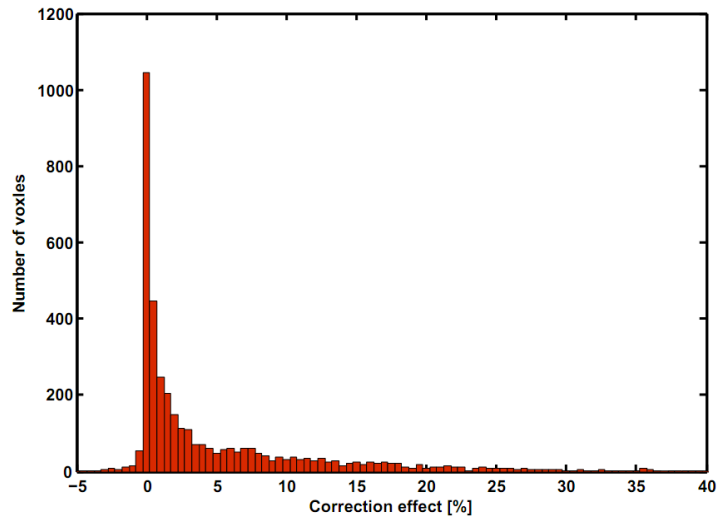
Figure 4.15: Histogram of the arterial dispersion correction effect on the absolute CBF for one subject.

4.5 Cerebral blood flow

Figure 4.16 displays CBF maps from all slices of one subject, calculated with the QUASAR methodology, and deconvolved with NSR, NSR_{CD} (NSR with correction for dispersion) and cSVD. It is obvious that cSVD generated higher CBF values in the peripheral GM regions. As an aid, Figure 4.17 displays a scatter plot of voxel values in the maps obtained by NSR_{CD} and cSVD.
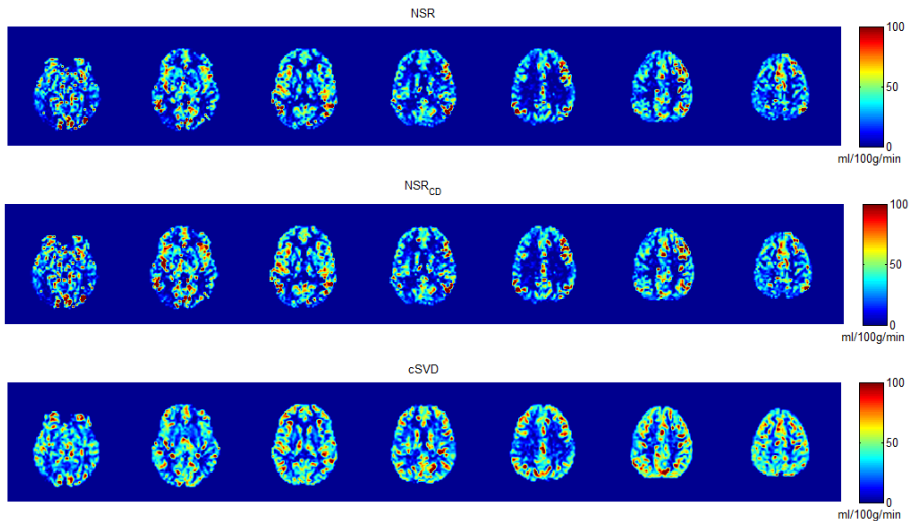

Figure 4.16: CBF maps as obtained by deconvolution with NSR (top), NSR_{CD} (middle) and cSVD (bottom).
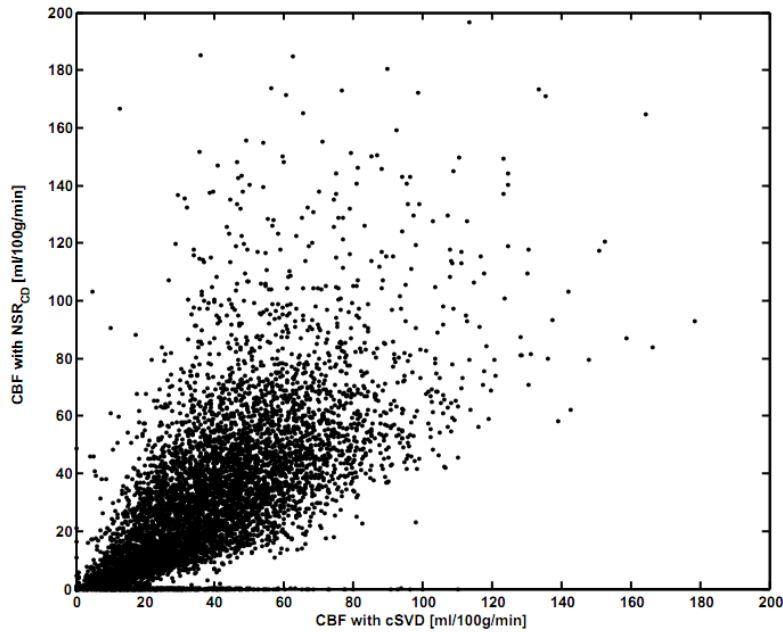
44

Figure 4.17: Scatter plot of CBF values voxel by voxel, as calculated by cSVD (x-axis) and NSR$_{CD}$ (y-axis).

The mean CBF in GM for all subjects was 37.9±6.1 ml/100g/min with no dispersion correction and 39.9±6.2 ml/100g/min with dispersion correction, as compared to cSVD deconvolution giving a mean CBF of 43.6±6.4 ml/100g/min for the same subjects. The absolute CBF calculated using NSR$_{CD}$ was 8.6% lower than for cSVD, although the difference is not statistically significant (p>0.05, two-sided t-test). Figure 4.18 displays the result, comparing NSR with cSVD, in a graph. Generally, NSR resulted in slightly lower CBF than cSVD when comparing each subject separately. The CBF is lower than expected from gold-standard methods for healthy volunteers (Leenders et al., 1990) and certainly seems to be underestimated.
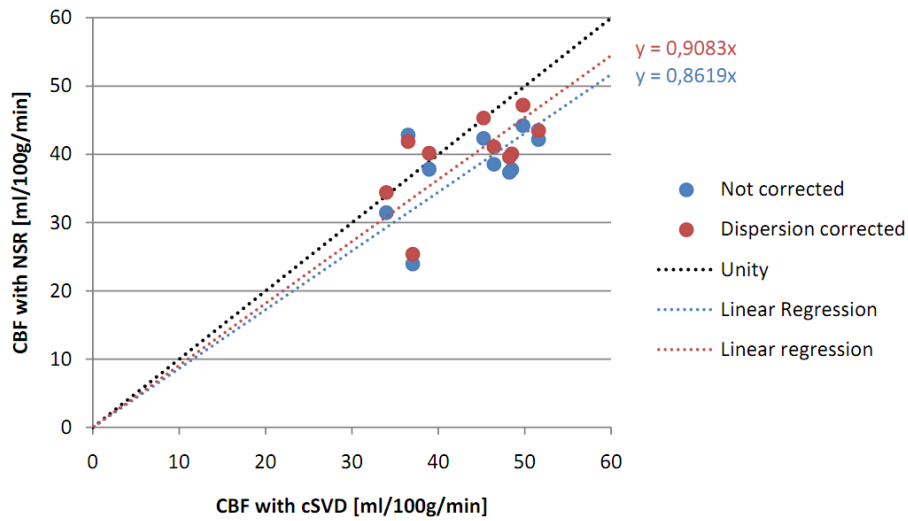
Figure 4.18: A graph comparing the CBF calculated with NSR deconvolution (y-axis) and cSVD deconvolution (x-axis). The CBF calculated with NSR is showed both with (red dots) and without (blue dots) correction for dispersion. The black dashed line is the line of identity, and the colored dashed are linear regressions (with a forced intercept equal to zero) corresponding to the data points of the same respective color.

Table 4.2 displays the calculated CBF in GM for the ten subjects in the study, with three different deconvolution variants, i.e., NSR, NSR_{CD} and cSVD. In the last column, the absolute CBF difference between NSR_{CD} and cSVD is shown.

Table 4.2: A summary of the results of the absolute CBF estimates. The last column compares NSR_{CD} with cSVD. All values are in ml/100g/min.

Subject	NSR	NSR_{CD}	cSVD	NSR_{CD} - cSVD
1	38.6	41.1	46.4	-5.3
2	31.5	34.4	34.0	0.5
3	23.9	25.4	37.0	-11.6
4	42.2	43.5	51.6	-8.1
5	37.8	40.2	38.9	1.3
6	42.4	45.3	45.2	0.1
7	44.2	47.2	49.8	-2.6
8	37.8	40.1	48.5	-8.4
9	37.4	39.6	48.2	-8.6
10	42.9	41.9	36.5	5.4
Mean	37.9	39.9	43.6	-3.7

4.6 ASL-NSR implementation

The result from the preliminary study of the delay sensitivity of NSR is shown in Figure 4.19. The NSR algorithm fails to reconstruct the tissue signal, potentially giving false CBF values, when the tissue signal arrives before the AIF (corresponding to negative shift values in Figure 4.19a). These negative delays seem to result in extremely overestimated CBF values. We also observed that, for positive shifts, the NSR algorithm usually reconstructs the residue function correctly, albeit shifted to the right corresponding to the delay. This is, however, only true for the dispersed residue function. One of the main advantages of NSR is the ability to reconstruct a residue function corrected for dispersion, but the results from this simulation suggest that an AIF delay can interfere with this correction, resulting in a residue function (and CBF) more similar to that of the uncorrected case. However, this test was more of a way to test how the algorithm handles shifted signals and the simulated delays in Figure 4.19a are quite exaggerated (corresponding to seconds in a DSC-MRI experiment). To test the impact of more realistic delays, in the order of a few seconds (Calamante et al., 2000), the tissue signal was shifted in smaller steps in Figure 4.19b. As indicated in the figures, the possibility to correct for dispersion seems to decrease as the arterial delay increases. Also, a small decrease in the uncorrected maximum value of the residue function is seen as the delay increases.
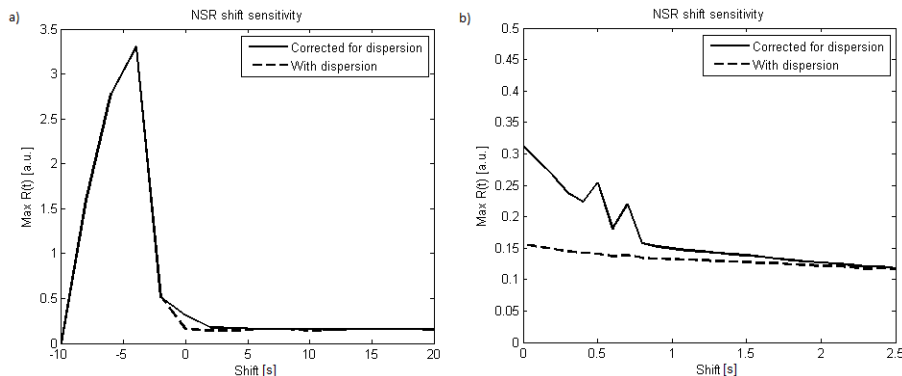

Figure 4.19: a) The maximum of the residue function as a function of the shift. Negative shift corresponds to a tissue signal starting before the arterial input function. A shift of zero corresponds to a tissue signal starting at the same time as the arterial input function, as expected when sampling an AIF close to the microvasculature. b) The maximum of the residue function as a function of smaller shifts. The vertical axis has the same arbitrary units as in a) to simplify comparison.

Finally, the implementation of an extra side constraint to minimize local increases of the solution proved to have potential. Preliminary results are encouraging since increasing as well as oscillating behavior of the solution is suppressed when the side constraint is used. Figure 4.20 displays an example of the potential impact of the side constraint. In the example, the implementation changed the (dispersion corrected) unrealistic solution into a physiologically realistic shape and generated an

almost identical reconvolved tissue signal. This means that the optimization has succeeded to minimize the increasing behaviour of the solution without the cost of a poorer correlation between measured data and the solution. However, the absolute CBF can change drastically when the new side constraint is used and therefore this implementation needs to be further verified.
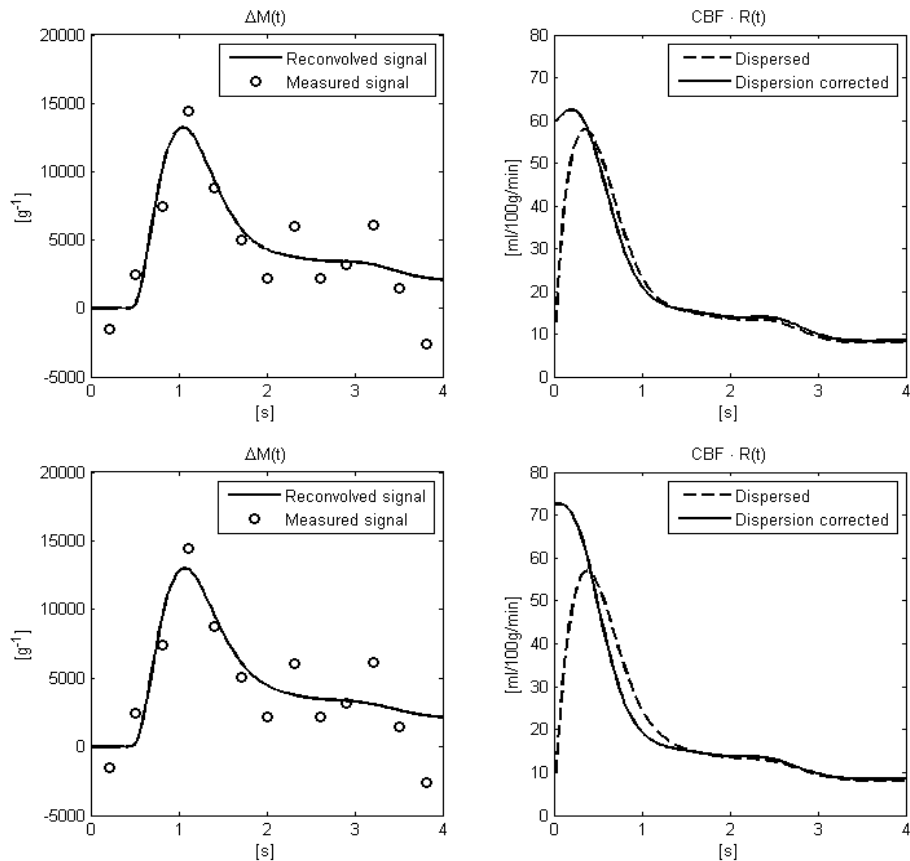
Figure 4.20: Impact of the additional side constraint on the monotonic decrease in a GM voxel. Top: Result from unmodified optimization showing non-physiological increase of the residue function. Bottom: Result from the same voxel, with inclusion of the additional side constraint minimizing the increasing behaviour of the solution. Figures on the left show measured tissue signal (ΔM) together with the reconvolved tissue signal, and figures on the right show $CBF \cdot R(t)$, with and without correction for dispersion.

5 Discussion

The application of NSR to time-resolved ASL data was feasible, although the resulting absolute CBF in GM was not entirely satisfactory since it was almost half of what is expected in healthy subjects, based on gold-standard methods (Leenders et al., 1990). The absolute CBF was, however, only slightly, and not significantly, lower than the CBF obtained by deconvolution with cSVD (Petersen et al., 2006a). The NSR implementation resulted in the possibility to study the residue function, $R(t) = r(t) \cdot m(t)$, in more detail than in most other time-resolved ASL experiments. Also, the implementation of a fractional segmentation was successful and resulted in realistic segmentations of the tissue types CSF, GM and WM without any need for additional imaging. The novel method for calculation of the equilibrium magnetization in arterial blood was implementable. The method generated homogeneous maps with values similar to those obtained by previously proposed methods (Petersen, 2009), but accounting for the amount of perfused tissue.

5.1   Fractional segmentation

The fractional segmentation, FRASIER, proved to be easily adaptable to the model-free ASL data, and to be able to differentiate between tissue types with great success. Maps of segmented tissues in form of fractional volumes were consistently realistic, although verification from, for example, an experienced radiologist would be beneficial. The segmentation method did not demand any prior information from the user, although T_1 in CSF was deliberately assumed to be 3 s since that value proved to be difficult to automatically obtain from the relaxation data. This assumption could be questioned, since many authors assume a longitudinal relaxation time of up to 4.5 s for CSF at 3T. However, the impact of this selection proved to be very small for the segmentation results, probably since the relaxation time difference between CSF and the parenchyma is large. The segmentation assumes that representative values of T_1 exist for the different tissue types. If, for example, a certain GM structure has a lower T_1 than the average value, FRASIER will misinterpret it to be a mixture of GM and WM (Shin et al., 2010). However, this is not necessarily a drawback compared to other methods since the majority of existing automatic segmentation algorithms assumes that the brain tissues have different representative relaxation parameters or MR signal/intensity.

The segmentation approach paved the way for a new method to estimate the equilibrium magnetization in arterial blood, by calculating both a weighted brain-blood partition coefficient and an equilibrium tissue magnetization excepting the signal from CSF. In addition, it proved to be a powerful tool when calculating mean parameters in different tissue types, most importantly CBF. Contrary to previous methods, the calculation of CBF in GM did not depend on a binary segmentation based on T_1 in tissue. Instead, the mean calculations could be easily varied with, for example, a threshold on the fractional volume of GM as the selective measure.

Previous studies have shown that CBF is largely underestimated in ASL experiments when including voxels only partially containing GM (Asllani et al., 2008). For example, including all voxels containing between 40% and 100% GM resulted in an underestimation on the CBF of about 50%. By choosing a high threshold of 80-90% fractional GM volume in order for a voxel to be included in the mean GM CBF calculation, underestimation can be avoided, or at least reduced. However, it also introduces larger errors since the number of voxels included in the quantification is significantly reduced (see Figure 5.1).
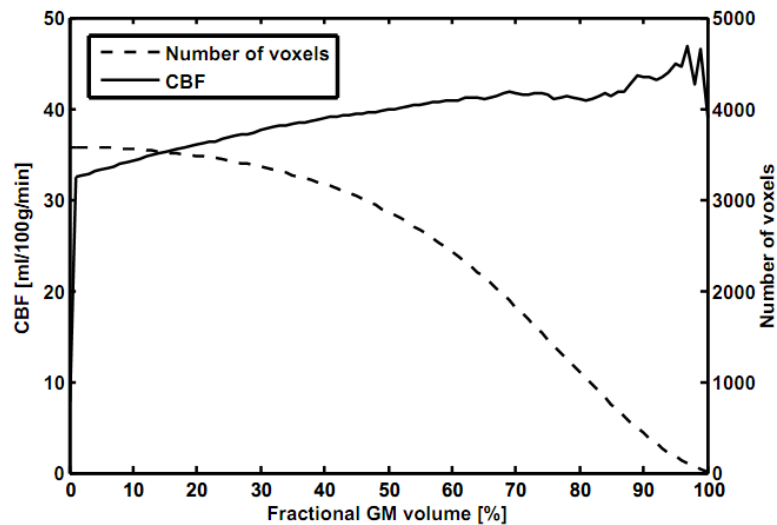

Figure 5.1: The partial volume effect on the CBF for one subject. The x-axis is the lower threshold on the fractional volume that is required for a voxel to be included in the calculation. The left y-axis is the CBF and the right y-axis is the number of voxels included in the CBF calculation for a certain threshold.

Some authors have suggested methods to correct the CBF for partial volume effects in ASL experiments (Asllani et al., 2008; Chappell et al., 2011). This is indeed very tempting since the resolution in most ASL experiments is poor. However, the suggested methods employ either local linear regression, resulting in a smoothing of the CBF map, or modelling of the kinetics with crude assumptions; assumptions that model-free ASL initially was created to avoid. However, using the fractional segmentation implemented in this study, it would be possible to solve the partial volume problem if CBF was measurable in WM, for example, by using a mixture model. Moving towards higher field strengths and newer ASL sequences with higher immanent SNR, the quantification of CBF in WM is likely to become feasible, potentially enabling direct correction for partial volume effects.

5.2 Estimation of $M_{0,a}$

Petersen et al. suggested exploiting the brain-blood partition coefficient to map $M_{0,a}$ including T_2^* effects across the brain to account for the T_2^* effects in ΔM (Petersen, 2009).The new method, presented in this study, builds on this approach and maps $M_{0,a}$ accounting for T_2^* effects, the variation of λ as well as partial volume effects of the apparent distribution volume. However, it uses the combined tissue magnetization of GM and WM, and not CSF. This could potentially introduce errors since the T_2^* effects are not fully accounted for. The T_2^* contrast from CSF is, however, expected to be small for a TE of 23 ms, since CSF has a long transverse relaxation time. If T_2^* in CSF could be quantified or estimated, the error could be reduced using $f_{s,CSF} \cdot e^{-TE/T_{2,CSF}^*}$.

The novel method for estimation of $M_{0,a}$ is to our knowledge the only one respecting the original definition of the brain-blood partition coefficient in ASL experiments. It interprets the brain-blood partition coefficient as the difference in distribution volumes of water between blood and perfused tissue, rather than the difference in proton density. The most widely used method is to use a global value of 0.9 ml/g or 0.98 ml/g for the partition coefficient, and compared to these methods, the new method is very different. The impact of the correction is, however, small with respect to the mean CBF, but could be important when studying regional CBF, especially in GM voxels with significant amount of CSF. The proposed method is also an improvement from the similar method 2 (see theory chapter) which uses a linear assignment of λ to the T_1 of tissue. This assumption of linearity is not needed in the novel method. Figure 5.2 displays difference maps between method 2 and the novel method. The underestimation when using method 2 is clear in voxels containing both GM and CSF. The error can yield an underestimation of several tens of percent depending on the fraction of GM and CSF in the specific voxel. The potential error of method 2 is not only the result of including CSF in the distribution volume, but also that the linear assignment of λ to the T_1 can result in extreme values of λ in voxels with CSF. For example, if T_1 is 1.5 s for GM, 1.0 s for WM and 4 s for CSF, then a voxel filled with 60% GM and 40% CSF would have an approximate partition coefficient of 0.59 ml/g, whereas method 2 would result in an estimated value of about 1.3 ml/g. The overestimation of the calculated CBF would partially be corrected for by the fact that method 2 includes the signal contribution from CSF, but even so the error could be several tens of percent.
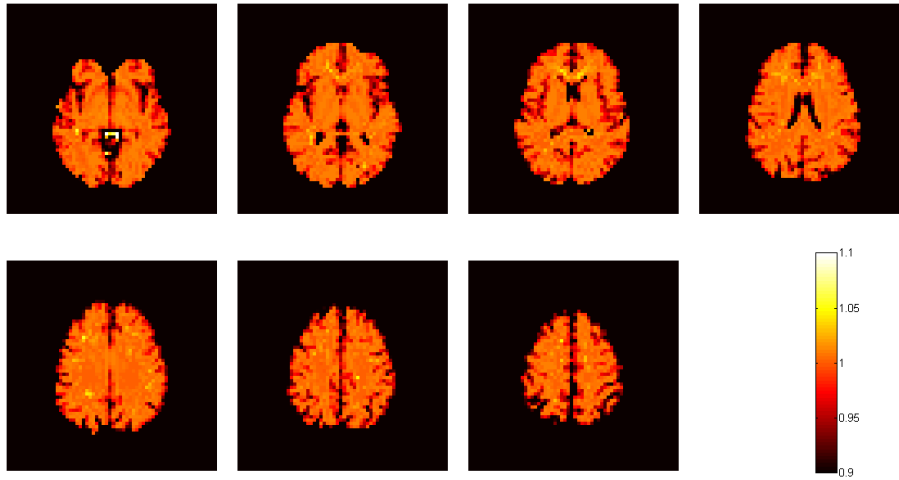
Figure 5.2: $M_{0,a}$ difference maps between method 2 and the novel method in one subject. Method 2 underestimates $M_{0,a}$ in voxels with partial CSF, most seriously in peripheral GM and GM close to the ventricles.

The new method assumes that the brain-blood partition coefficient only varies with tissue type. Herscovitch and Raichle showed that water content also varies among different GM structures and WM regions (Herscovitch and Raichle, 1985). Different GM structures can have a partition coefficient varying between 0.88 and 0.99 ml/g, and different WM regions show a range of 0.83-0.96 ml/g, with respective means of 0.98 ml/g and 0.82 ml/g. Since λ scales $M_{0,a}$, which in return scales CBF, an error in the partition coefficient transfers linearly (in an inverse manner) to the CBF. The use of an estimated mean GM partition coefficient of 0.98 ml/g could result in a 10% underestimation of the CBF in certain GM structures with particularly low water content. These errors could be avoided by assigning different partition coefficients to different structures and regions, but it would be difficult without demanding user input.

The use of the brain-blood partition coefficient is only valid if the blood-tissue exchange of water is instantaneous upon arrival to the capillary system. Many studies have shown that water is not a freely diffusible tracer. The QUASAR implementation avoids the use of compartment models to describe the water exchange between blood and tissue, by sampling the shape of the arterial function. However, by using the partition coefficient in the calculation of $M_{0,a}$, the assumption of free diffusibility remains. Also, λ depends on the hematocrit level of the blood, which shows low intra subject variation but differences between different individuals can be significant (Herscovitch and Raichle, 1985). One way to minimize this error, as well as the intra brain variability of λ between different structures and regions, would be to implement a sequence capable of measuring the proton density and mapping the brain-blood partition coefficient for each subject.

5.3   Residue function characteristics

The resolved residue functions showed very satisfying characteristics with generally non-negative, non-oscillating and monotonically decreasing behaviour. It is very encouraging that NSR, with some modifications, was smoothly adoptable from DSC-MRI to model-free ASL, especially since ASL has poorer SNR and fewer sampling points during the bolus passage. Also, the propagation of the tracer bolus, the kinetic response and the different sampling frequency and total time span differ substantially between the two perfusion quantification methods. For example, after the labelling, model-free ASL performs imaging for about 4 seconds with around 300-400 ms sampling frequency, whereas a DSC-MRI experiment often lasts for around 1 minute with a sampling frequency of 1-2 seconds.

The implementation resulted mostly in smooth, non-oscillating and non-negative residue functions with physiologically realistic shapes. However, it also showed examples of non-monotonically decreasing residue functions, as well as other non-physiological shapes. It is not straightforward to point out exactly why the implementation is not entirely robust, but some reasons can be presumed. The error in the measured MR signal is probably the most limiting factor in an ASL experiment. In almost all cases when the residue function displayed unrealistic shapes, the tissue signal was very noisy. If the optimization minimizes the deviation between measured signal and the solution well enough, it risks to largely ignore the side constraint which exists only to obtain physiologically realistic and smooth shapes. Improving the modelling of the measurement noise in the NSR implementation might be the most important work in future optimizations.

Among the advantages of NSR is that it recreates the residue function with a virtually high temporal resolution which is helpful when studying the characteristics of the kinetic curves. However, this demands that the AIF is defined on the same time grid, implying that the measured input signal needs to be fitted to a parametric function if a time resolution finer than that of the measurement is desired. Choosing the gamma-variate as a parametric function assumes that the bolus of labelled spins has been largely dispersed, traveling from the labelling site to the tissue feeding artery, since the initial bolus has an almost rectangular shape. The gamma-variate can be questioned since a dispersed rectangular shape, including relaxation of the labelled blood water, is not necessarily best described by this parameterization. As an example, Figure 5.3 displays how both a gamma variate and a very different parametric function (based on a theorized bolus deformation) can show a fairly good fit to the data, and still present very different shapes. The alternative parameterization starts with an ideal bolus of the predefined length, which is then dispersed by deconvolution with a first order transport function, and multiplied with a relaxation function. This model is very rough and is not suggested as an alternative since it is not verified and probably less robust, but rather as a comparing example of the variety of possible AIF shapes. Repeating experiments with inversion times changed in small increments would allow a higher temporal resolution, potentially enabling a good choice of the parameterization by studying general shapes of input functions in large vessels.
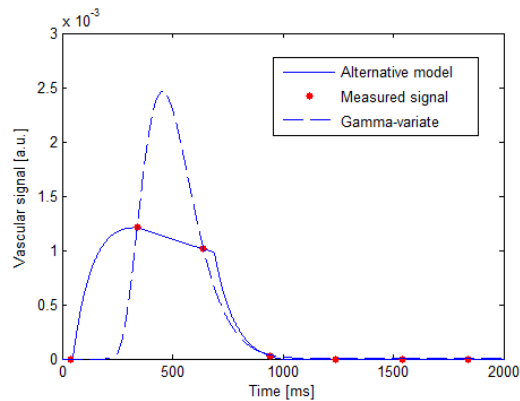
Figure 5.3: Alternative parameterizations of the AIF can result in very different shapes. Red dots are the measured signal in a voxel identified as an AIF.

Figure 4.13 showed examples of resulting NSR parameter maps of θ_1, θ_2 and θ_3, but it is clearly difficult to deduce any valuable information from these maps. The parameter relating to the measurement noise, θ_3, is expected to be fairly constant between tissue types since it only reflects the noise level (Zanderigo, 2006). Zanderigo et al. pointed out that θ_1 maps (dispersion) could potentially be used as an indicator of pathological tissue, as a complement to the other haemodynamic parameters such as CBF, CBV, MTT (Zanderigo et al., 2009). However, our study uses a nosier perfusion MRI method and no global AIF, which means that the dispersion is more difficult to quantify and interpret. As a future investigation it would be interesting to use NSR in model-free ASL with a global AIF to see if the θ_1 map would contain any information about the arterial dispersion in ASL, for example in patients with known stenosis.

Whereas the calculated CBF did not seem to change significantly with the new implementation, deconvolution with NSR surpasses cSVD largely when looking at the recreation of a voxel-wise residue function. Figure 4.14 displayed a comparison of the residue function characteristics between deconvolution by NSR and cSVD. Whereas NSR succeeded to resolve smooth realistic residue functions in most cases, cSVD consequently generated non-physiological oscillating and negative solutions. The large oscillations of cSVD generally seem to depend on "overfitting" of the tissue signal. Since the tissue signal is very noisy in the ASL experiment, cSVD performs poorly considering residue function characteristics. The only way to avoid oscillations in cSVD is to set an even more narrow threshold, with the risk of largely underestimating the CBF.

It is easy to get carried away by the beautiful results emerging from NSR, but one should certainly exercise some degree of caution. One of the main motivations of NSR is that it respects the definitions of the residue function as defined in the indicator-dilution theory proposed by Meier and Zierler (Zierler, 1962). However, these definitions are based on capillary systems rather than voxels (although the typical interpretation is to look at the residue function as the fraction of labelled

54

spins that still remains in the voxel rather than within the capillary system at a specific time), and also that input and output functions are ideal, which is not the case in practice. Since it is impossible to measure a true AIF at the entrance of a capillary system and at the same time couple it with the signal from that capillary system, it is possible that NSR generates realistic residue functions at the cost of being more or less incorrect.

5.4 Arterial dispersion correction

Our hypothesis was that the deconvolution with cSVD was a significant reason for the underestimation of CBF in model-free ASL, and therefore that the application of an alternative deconvolution method could improve the absolute quantification. For example, cSVD underestimates the CBF if the arterial dispersion is significant (Calamante et al., 2000), whereas NSR can correct for arterial dispersion (Zanderigo, 2006). However, dispersion of the bolus from the measurement site of the AIF to the capillary system is expected to be small in an experiment employing local AIFs. Furthermore, many authors have described more complex modelling of arterial dispersion in ASL (Gallichan and Jezzard, 2008; Kazan et al., 2009) and the NSR implementation would probably benefit from replacing the first approximation of the vascular transport function with a more realistic model, preferably together with a more realistic parameterization of the AIF.

The most interesting result from the study of the effect of the dispersion correction was that about half of the GM voxels had a noticeable dispersion effect (>1%) and that the mean effect in these GM voxels was approximately 10%. This result could imply that dispersion is not negligible even when employing local AIFs, and that correction is of importance in the quantification, especially in regions far from a measureable input function. Also, the histogram in Figure 4.15 shows that the dispersion correction can have an effect on the CBF of several tens of percent. These voxels or regions correspond logically to areas with large dispersion, as identified by NSR.

The authors of the model-free ASL implementation and the QUASAR sequence, primarily Petersen and Golay, have pointed out the importance of dispersion, as well as analyzed its impact on the perfusion quantification using QUASAR (Petersen and Golay, 2010). They showed that QUIPSSII is robust to dispersion but that the quantification of arrival time is affected by dispersion. Furthermore, they suggested the use of the Gaussian dissipation function, rather than the gamma variate, to parameterize the vascular signal. They also showed that unexpected bolus shortening, i.e., the AIF bolus length being shorter than the nominal bolus length (640 ms in this work), could be a related source of error. This effect was more frequent than expected, resulting in large underestimations of the CBF.

In conclusion, the dispersion correction had an effect on the resulting CBF in GM, although the effect was small (mean 6% for GM). Arterial dispersion is therefore probably not the main reason for the underestimation of CBF in GM in model-free ASL.

5.5 Cerebral blood flow

As pointed out several times above, the calculated CBF estimates in GM were lower than expected for normal volunteers. The study aimed at improving the quantification of CBF by model-free ASL, which previously has resulted in CBF at the lower end of previously published values. Different versions of the QUASAR sequence have rendered CBF values in GM from 38 to 47 ml/100g/min (Petersen et al., 2006a; Petersen et al., 2010). Petersen et al. pointed out that their results are close to the values obtained using similar acquisition techniques and within the range of previously published values (Petersen, 2009). They suggest that the reason for their values being low compared to many literature values could be that QUASAR calculates CBF in a full brain GM ROI, whereas many other studies uses small hand drawn ROIs, and that the regularization technique generally underestimates CBF. Furthermore, the use of crusher gradients eliminate signal from fast-flowing blood in arteries and arterioles, potentially generating lower CBF estimates than other imaging modalities in which that signal is present (Knutsson et al., 2010).

The resulting CBF in GM from this study was 39.9±6.2 ml/100g/min and is consequently also within the range of published QUASAR values. However, it is not possible to neglect that the result is significantly lower than those from gold standard techniques. A standard reference is Leenders et al., who published a mean GM CBF of 54.8±12.0 ml/100g/min obtained with the ^{15}O steady-state inhalation method (PET), in 34 healthy volunteers (Leenders et al., 1990). The true CBF in GM is often stated to be even higher, about 60-70 ml/100g/min (acknowledging that Leenders et al. did not correct for GM/WM partial volume effects).

One main difference between NSR and cSVD is that NSR generated very low or zero CBF values in many voxels in which cSVD showed higher values (Figure 5.4). This depended on the noise in the tissue signal. If NSR cannot find any fitting solution, it optimizes fully on the side constraint, which means that the solution becomes the most regular and smooth shape that is mathematically possible, i.e., a straight line. This constant is most often zero or close to zero, and therefore the estimated CBF is zero. In contrast, cSVD deconvolution, with the same AIF and tissue signal, will in almost all cases generate a higher value. Looking at the residue function from this calculation it is clear that cSVD generates highly unrealistic, oscillating solutions, especially when the measured signal is noisy. Since the solution has an oscillating shape, the calculated CBF will be the maximum value of this function. These voxels should preferably be omitted when calculating the mean CBF in GM. However, the present implementation of NSR also overestimates the CBF in some voxels and considering both under- and overestimation of NSR and cSVD, the results do not differ significantly. The overestimation in some voxels seems to originate from delays not manageable by the automatic shift algorithm. As mentioned earlier, a negative shift (i.e., an AIF arriving after the starting edge of the tissue signal) can introduce extreme overestimations of the CBF.
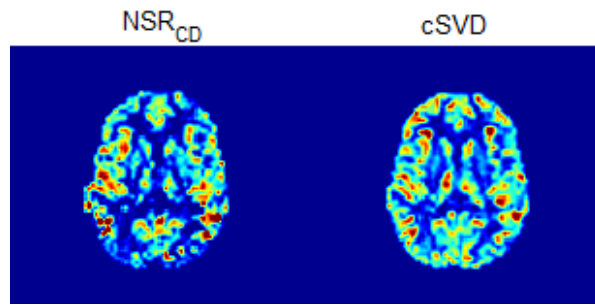
Figure 5.4: Comparison of CBF maps obtained by deconvolution with NSR_{CD} (left) and cSVD (right). NSR_{CD} has regions with low CBF values compared to cSVD, which probably is underestimation (or optimization failure), primarily due to poor SNR.

In addition to the differences between NSR and cSVD mentioned above, the methods seem to perform very differently as seen in the scatter plot in Figure 4.17. The overall higher CBF values for cSVD are seen in the plot, and also the great number of voxels with zero CBF for NSR as well as the absence of such voxels for cSVD. This emphasizes that NSR fails to calculate the CBF in voxels with too noisy tissue signals and that cSVD probably has large errors in the calculated CBF in the same voxels.

Movement during and between acquisitions can be a significant source of error in the CBF quantification. The pulse sequence lasts for 6 min with 84 different acquisitions. Errors introduced by movement are particularly important when calculating CBF voxel-by-voxel. As mentioned earlier, many authors use ROIs to represent a particular tissue, and this study could potentially benefit from the use of mean dynamic curves including neighboring voxels (in plane). Better yet, a movement correction is capable of reducing errors due to movement and such an implementation could be considered in the future.

5.6 Delay sensitivity

It is clear that NSR is sensitive to arterial delay. The preliminary investigation showed that it is essential for the AIF and the tissue signal to have realistic starting edges in relation to each other, i.e., that they start almost simultaneously, and that the calculated CBF depends on the delay. The result was undesired but encouraged the implementation of a shift optimization algorithm, which also proved to result in a higher frequency of physiologically realistic residue functions in general. The delay sensitivity was primarily a concern for the dispersion-corrected residue functions. Large arterial delays tended to reshape the corrected residue functions into looking more like the corresponding dispersed curves. As mentioned earlier, the dispersion effect when measuring local AIFs is expected to be small, and therefore the delay sensitivity would not primarily be an issue for the CBF quantification, but rather the validity of the residue function characteristics. However, for patients where an AIF is not available close to the pathology, the delay sensitivity can be of significance for the perfusion quantification.

5.7 ASL-NSR implementation

The complexness of the NSR algorithm made it somewhat difficult to implement in for data that are very different from the DSC-MRI data for which it was originally intended. To obtain realistic solutions with ASL data, several modifications had to be tested and optimized. Among those was the modelling of the measurement noise. Without this modification it was impossible to obtain any good results from the deconvolution. Also, the starting parameters of NSR had to be tested for a variety of different tissue and vascular signals to find the optimal values.

Several things remain to be optimized in the implementation. For example, the number of eigenvalues and eigenvectors were fixed at 10 during the whole study. A minor test showed that the number could affect the CBF, and this number should be optimized to obtain acceptably small errors without too large computational cost. Furthermore, it is important to investigate the selection of NSR starting values. For this study, initial manual variation, followed by visual inspection of the result, served as a subjective method to find optimal starting values that worked for a wide variety of input signals. It is difficult to find general starting parameters that work for all subjects and voxels, and a future improvement could be to automatically analyze the tissue and arterial signal prior to the deconvolution, and chose a unique set of starting parameters based on the shape and on empirical experience.

We chose to abandon the measurement noise modelling that was initially suggested in NSR (Zanderigo, 2006), and instead exploited the fact that the ASL sequence utilizes repeated measurements, enabling estimation and mapping of the measurement noise through the population standard deviation. This proved to be an essential modification to obtain reasonable residue function solutions. Zanderigo et al. posed that the noise level in the measurement was proportional to the inverse of the tissue signal intensity (Zanderigo, 2006), which proved to be successful in the DSC-MRI case. For model-free ASL, averaging is required due to the low perfusion signal. Therefore it is more natural to assume that the noise level is proportional to the standard deviation, rather than to the resulting mean value.

Among the modifications was also the implementation of a measure of the monotonic decrease of the solution, as an extra side constraint in the optimization process of NSR. The implementation proved to be able to suppress oscillating behavior of residue functions but it was never rigorously verified and therefore left out of the deconvolution process for the time being. It was clear that the side constraint generally minimized oscillations in the solution, but it was not made clear whether the modification could bias the CBF calculation. It would have to be verified that the CBF is not under- or overestimated, but rather corrected, when using the modification. Further testing and optimization of this side constraint could potentially improve CBF quantification with the ASL-NSR implementation.

6 Conclusion

Non-linear stochastic regularization as a deconvolution method for absolute quantification of cerebral blood flow using model-free arterial spin labelling data has been evaluated. The implementation resulted in realistic residue functions with promising potential to quantify the cerebral blood flow in grey matter. Residue functions were smooth, non negative and reconstructed on a virtual time grid with a high temporal resolution. The study also brought on the successful implementation of a fractional segmentation, enabling flexible calculations of mean values of different parameters in grey matter and white matter. The fractional segmentation formed the basis for a novel method for the estimation of the equilibrium magnetization of arterial blood which is an essential parameter for the perfusion quantification in ASL. The equilibrium magnetization of arterial blood scales the CBF linearly, and the new method could potentially avoid underestimation of the CBF, particularly in areas with high (voxel-wise) mixture of grey matter and CSF. The possibility to correct for arterial dispersion, inherent to the NSR algorithm, proved to have a significant effect on the quantification, even though model-free ASL employs local arterial input functions. The underestimation of the perfusion due to arterial dispersion has been discussed thoroughly in the literature, and a possibility to model and correct for it would be a huge step forward in the process of improving ASL quantification of perfusion.

A lot of work remains for NSR to become an as powerful tool as in DSC-MRI. The implementation demanded several modifications which are not finalized regarding optimization and verification. Among the most obvious topics are the measurement noise modelling, the selection, fitting and averaging of arterial input functions, the shift of the dynamic curves (or equivalently minimizing the delay sensitivity of NSR) and the variability of NSR, such as starting parameters, implementation of extra side constraints, number of eigenvalues/eigenvectors and the virtual time resolution. The calculation of fundamental parameters such as the brain-blood partition coefficient, the equilibrium magnetization and relaxation time in arterial blood and the inversion efficiency, are also subject to potential improvements. Future possible improvements also include optimizing the computational cost of NSR, since a calculation of one session can take several hours on a standard PC.

Together with expected improvements of, for example, correction for partial volume effects, ability to measure CBF in white matter, controlling arterial input functions and correction for unexpected bolus reduction, NSR could potentially have an important role in perfusion quantification using time-resolved ASL. The results of this work can hopefully be of value for understanding the underlying processes of the haemodynamics and kinetic responses in ASL experiments.

Acknowledgements

References

Andersen IK, Szymkowiak A, Rasmussen CE, Hanson LG, Marstrand JR, Larsson HBW, Hansen LK. Perfusion quantification using Gaussian process deconvolution. *Magnetic Resonance in Medicine* 2002;48:351-361.

Asllani I, Borogovac A, Brown TR. Regression algorithm correcting for partial volume effects in arterial spin labeling MRI. *Magnetic Resonance in Medicine* 2008;60:1362-1371.

Bell B, Pillonetto G. Estimating parameters and stochastic functions of one variable using nonlinear measurements models. *Inverse Problems* 2004;20:627-646.

Buxton RB, Frank LR, Wong EC, Siewert B, Warach S, Edelman RR. A general kinetic model for quantitative perfusion imaging with arterial spin labeling. *Magnetic Resonance in Medicine* 1998;40:383-396.

Calamante F, Gadian DG, Connelly A. Delay and dispersion effects in dynamic susceptibility contrast MRI: Simulations using singular value decomposition. *Magnetic Resonance in Medicine* 2000;44:466-473.

Calamante F, Gadian DG, Connelly A. Quantification of bolus-tracking MRI: Improved characterization of the tissue residue function using Tikhonov regularization. *Magnetic Resonance in Medicine* 2003;50:1237-1247.

Chappell MA, Groves AR, MacIntosh BJ, Donahue MJ, Jezzard P, Woolrich MW. Partial volume correction of multiple inversion time arterial spin labeling MRI data. *Magnetic Resonance in Medicine* 2011;65:1173-1183.

de Nicolao G, Sparacino G, Cobelli C. Nonparametric input estimation in physiological systems: Problems, methods, and case studies. *Automatica* 1997;33:851-870.

Detre JA, Leigh JS, Williams DS, Koretsky AP. Perfusion imaging. *Magnetic Resonance in Medicine* 1992;23:37-45.

Donahue MJ, Lu H, Jones CK, Edden RA, Pekar JJ, van Zijl PC. Theoretical and experimental investigation of the VASO contrast mechanism. *Magnetic Resonance in Medicine* 2006;56:1261-1273.

Edelman RR, Siewert B, Darby DG, Thangaraj V, Nobre AC, Mesulam MM, Warach S. Qualitative mapping of cerebral blood flow and functional localization with echo-planar MR imaging and signal targeting with alternating radio frequency. *Radiology* 1994;192:513-520.

Gallichan D, Jezzard P. Modeling the effects of dispersion and pulsatility of blood flow in pulsed arterial spin labeling. *Magnetic Resonance in Medicine* 2008;60:53-63.

Golay X, Petersen ET, Hui F. Pulsed star labeling of arterial regions (PULSAR): A robust regional perfusion technique for high field imaging. *Magnetic Resonance in Medicine* 2005;53:15-21.

Herscovitch P, Raichle ME. What is the correct value for the brain-blood partition coefficient for water? *Journal of Cerebral Blood Flow & Metabolism* 1985;5:65-69.

Hill L. The physiology and pathology of the cerebral circulation: An experimental research. J. & A. Churchill, London 1896.

Kazan SM, Chappell MA, Payne SJ. Modeling the effects of flow dispersion in arterial spin labeling. *IEEE Transactions on Biomedical Engineering* 2009;56:1635-1643.

Kety SS, Schmidt CF. The determination of cerebral blood flow in man by the use of nitrous oxide in low concentrations. *American Journal of Physiology* 1945;143:53-66.

Kety SS, Schmidt CF. The nitrous oxide method for the quantitative determination of cerebral blood flow in man: Theory, procedure and normal values. *The Journal of Clinical Investigation* 1948;27:476-483.

Kim SG. Quantification of relative cerebral blood flow change by flow-sensitive alternating inversion recovery (FAIR) technique: Application to functional mapping. *Magnetic Resonance in Medicine* 1995;34:293-301.

Knutsson L, van Westen D, Petersen ET, Bloch KM, Holtas S, Stahlberg F, Wirestam R. Absolute quantification of cerebral blood flow: Correlation between dynamic susceptibility contrast MRI and model-free arterial spin labeling. *Magnetic Resonance Imaging* 2010;28:1-7.

Kwong KK, Belliveau JW, Chesler DA, Goldberg IE, Weisskoff RM, Poncelet BP, Kennedy DN, Hoppel BE, Cohen MS, Turner R, et al. Dynamic magnetic resonance imaging of human brain activity during primary sensory stimulation. *Proceedings of the National Academy of Sciences USA* 1992;89:5675-5679.

Kwong KK, Chesler DA, Weisskoff RM, Donahue KM, Davis TL, Østergaard L, Campbell TA, Rosen BR. MR perfusion studies with T1-weighted echo planar imaging. *Magnetic Resonance in Medicine* 1995;34:878-887.

Leenders KL, Perani D, Lammertsma AA, Heather JD, Buckingham P, Healy MJ, Gibbs JM, Wise RJ, Hatazawa J, Herold S, et al. Cerebral blood flow, blood volume and oxygen utilization. Normal values and effect of age. *Brain* 1990;113 (Pt 1):27-47.

Look DC, Locker DR. Time saving in measurement of NMR and EPR relaxation times. *Review of Scientific Instruments* 1970;41:250-251.

Lu H, Clingman C, Golay X, van Zijl PCM. Determining the longitudinal relaxation time (T1) of blood at 3.0 Tesla. *Magnetic Resonance in Medicine* 2004;52:679-682.

Luh WM, Wong EC, Bandettini PA, Hyde JS. QUIPSS II with thin-slice TI1 periodic saturation: A method for improving accuracy of quantitative perfusion imaging using pulsed arterial spin labeling. *Magnetic Resonance in Medicine* 1999;41:1246-1254.

Parker DL, Christian BA, Goodrich KC, Alexander AL, Buswell HR, Yoon C. Improved accuracy in T1 measurements. *Proceedings of the 6th Annual Meeting of ISMRM*, Sydney, Australia 1998 (#2172).

Petersen ET. Brain perfusion imaging: Quantification of cerebral blood flow using ASL techniques. Ph.D. Thesis. Faculty of Health Sciences, Aarhus University, 2009.

Petersen ET, Golay X. The effect of bolus length and dispersion on arterial spin labeling flow quantification *Proceedings of the 19th Annual Meeting of ISMRM*, Stockholm, Sweden 2010 (#514).

Petersen ET, Lim T, Golay X. Model-free arterial spin labeling quantification approach for perfusion MRI. *Magnetic Resonance in Medicine* 2006a;55:219-232.

Petersen ET, Mouridsen K, Golay X. The QUASAR reproducibility study, Part II: Results from a multi-center arterial spin labeling test-retest study. *Neuroimage* 2010;49:104-113.

Petersen ET, Zimine I, Ho YC, Golay X. Non-invasive measurement of perfusion: A critical review of arterial spin labelling techniques. *The British Journal of Radiology* 2006b;79:688-701.

Pillonetto G, Sparacino G, Cobelli C. Handling non-negativity in deconvolution of physiological signals: A nonlinear stochastic approach. *Annals of Biomedical Engineering* 2002;30:1077-1087.

Roberts DA, Rizi R, Lenkinski RE, Leigh JS, Jr. Magnetic resonance imaging of the brain: Blood partition coefficient for water: Application to spin-tagging measurement of perfusion. *Journal of Magnetic Resonance Imaging* 1996;6:363-366.

Shin W, Geng X, Gu H, Zhan W, Zou Q, Yang Y. Automated brain tissue segmentation based on fractional signal mapping from inversion recovery Look-Locker acquisition. *Neuroimage* 2010;52:1347-1354.

Traystman RJ. The paper that completely altered our thinking about cerebral blood flow measurement. *Journal of Applied Physiology* 2004;97:1601-1602.

Williams DS, Detre JA, Leigh JS, Koretsky AP. Magnetic resonance imaging of perfusion using spin inversion of arterial water. *Proceedings of the National Academy of Sciences USA* 1992;89:212–216.

Wirestam R, Ståhlberg F. Wavelet-based noise reduction for improved deconvolution of time-series data in dynamic susceptibility-contrast MRI. *Magnetic Resonance Materials in Physics, Biology and Medicine* 2005;18:113-118.

Wong EC, Buxton RB, Frank LR. Quantitative imaging of perfusion using a single subtraction (QUIPSS and QUIPSS II). *Magn Reson Med* 1998;39:702-708.

Wu O, Østergaard L, Weisskoff RM, Benner T, Rosen BR, Sorensen AG. Tracer arrival timing-insensitive technique for estimating flow in MR perfusion-weighted imaging using singular value decomposition with a block-circulant deconvolution matrix. *Magnetic Resonance in Medicine* 2003;50:164-174.

Wu WC, Fernandez-Seara M, Detre JA, Wehrli FW, Wang J. A theoretical and experimental investigation of the tagging efficiency of pseudocontinuous arterial spin labeling. *Magnetic Resonance in Medicine* 2007;58:1020-1027.

Ye FQ, Mattay VS, Jezzard P, Frank JA, Weinberger DR, McLaughlin AC. Correction for vascular artifacts in cerebral blood flow values measured by using arterial spin tagging techniques. *Magn Reson Med* 1997;37:226-235.

Zanderigo F. Assessment of cerebral hemodynamics by deconvolution with dynamic susceptibility contrast - magnetic resonance imaging. Ph.D. Thesis. Faculty of Engineering, University of Padua, 2006.

Zanderigo F, Bertoldo A, Pillonetto G, Cobelli Ast C. Nonlinear stochastic regularization to characterize tissue residue function in bolus-tracking MRI: Assessment and comparison with SVD, block-circulant SVD, and Tikhonov. *IEEE Transactions on Biomedical Engineering* 2009;56:1287-1297.

Zierler KL. Theoretical basis of indicator-dilution methods for measuring flow and volume. *Circulation research* 1962;10:393-407.

Zierler KL. Equations for measuring blood flow by external monitoring of radioisotopes. *Circulation research* 1965;16:309-321.

Østergaard L, Weisskoff RM, Chesler DA, Gyldensted C, Rosen BR. High resolution measurement of cerebral blood flow using intravascular tracer bolus passages. Part I: Mathematical approach and statistical analysis. *Magnetic Resonance in Medicine* 1996;36:715-725.

Appendix I. Abstract accepted at ESMRMB11

Resolving the Residue Function in Model-Free Arterial Spin Labeling using Non-Linear Stochastic Regularization

A. Ahlgren[1], R. Wirestam[1], F. Ståhlberg[1,2], L. Knutsson[1]

[1]Dept. of Medical Radiation Physics, Lund University, Lund, Sweden
[2]Dept. of Diagnostic Radiology, Lund University, Lund, Sweden

Introduction
QUASAR model-free Arterial Spin Labeling (ASL) has been applied to quantification of Cerebral Blood Flow (CBF) [1]. Block-circulant singular value decomposition (cSVD) for deconvolution [2] is often associated with non-physiological (oscillating and negative) residue functions and potential effects of arterial dispersion [3,4]. Non-Linear Stochastic Regularization (NSR) has previously been used to reproduce realistic residue functions in dynamic susceptibility contrast MRI, including correction for arterial dispersion [5]. To characterize the residue function R(t) in model-free ASL, and possibly to improve absolute CBF quantification, NSR was applied to deconvolution of QUASAR data.

Subjects and Methods
Data from volunteers participating in the QUASAR reproducibility study were analyzed [6]. Imaging was carried out using Philips Achieva 3T MRI: $TR/TE/\Delta TI/TI_1 = 4000/23/300/40$ ms, 64x64 matrix, 7 slices and 13 inversion times. The tissue perfusion signal $\Delta M(t)$ and the arterial input function AIF(t) were calculated similarly to ref. [1], and CBF·R(t) was obtained according to $\Delta M(t) = CBF \cdot R(t) \otimes AIF(t)$. The required deconvolution was performed using NSR [5], i.e. a stochastical interpretation of Tikhonov regularization with R(t) modelled by multiple integration of a random-walk process.
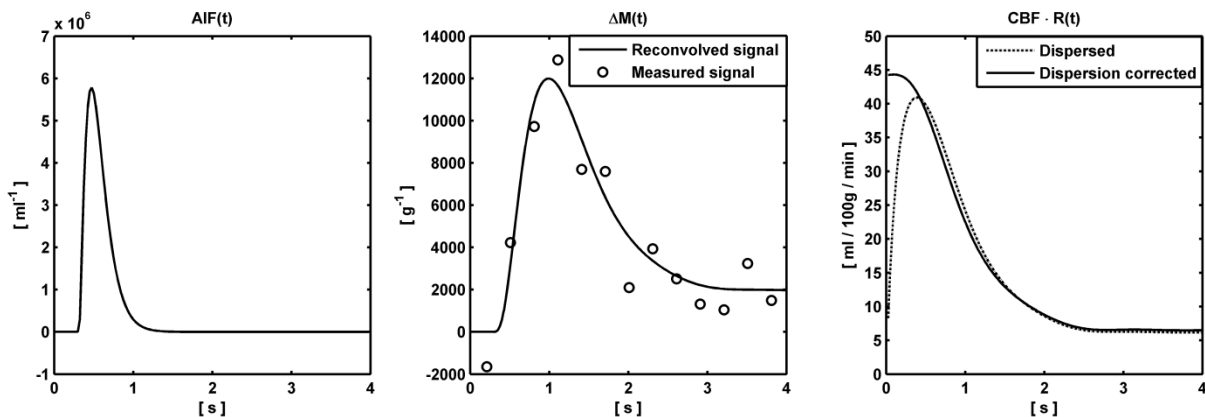

Figure 1. *Left:* Gamma-variate fitted arterial input function. *Middle:* Measured and reconvolved tissue signal. *Right:* Residue function.

Results
Figure 1 shows R(t) for a grey-matter (GM) voxel, with/without dispersion correction, as well as the fitted AIF(t) and the measured and reconvolved $\Delta M(t)$ data. NSR consistently resolved realistic, non-negative residue functions, with little or no oscillations, from time-resolved ASL data. Figure 2 shows a CBF map from one subject. The effect of dispersion correction was analyzed for GM in one subject. In 45% of the voxels, the dispersion correction had negligible effect (<1%) on the peak R(t) value. For the remaining voxels, the peak R(t) value was $(10\pm16)\%$ (mean±SD) higher after dispersion correction, with 57% of these voxels showing a dispersion correction effect exceeding 5%. NSR returned a GM CBF of (40.5±5.1) ml/100g/min (n=9), while the corresponding result for cSVD was (44.0±7.0) ml/100g/min.

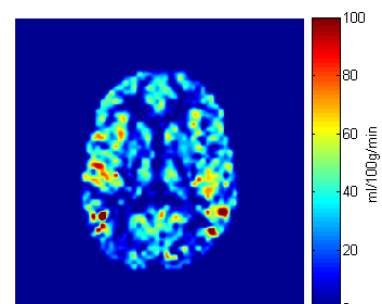**Figure 2.** CBF in a middle brain slice.

Discussion
Residue functions resolved by NSR satisfactorily meet the criteria of non-negativity and monotonic decrease, making NSR superior for investigating the physiological dynamics of brain perfusion. To further optimize absolute CBF quantification, future investigations will deal with optimization of NSR starting values and evaluation of delay sensitivity.

References
[1] Petersen ET et al., 2006, MRM, 55:219-232. [2] Wu O et al., 2003, MRM, 50:164-174. [3] Petersen ET et al., 2010, Proc 18th ISMRM, #514. [4] Calamante F et al., 2000, MRM, 44:466-473. [5] Zanderigo F et al., 2009, IEEE T Bio-Med Eng, 56:1287-1297. [6] Petersen ET et al., 2010, NeuroImage, 49:104-113.

Appendix II. Abstract accepted at ESMRMB11

Using Fractional Segmentation for Estimation of the Equilibrium Magnetization of Arterial Blood in Model-Free Arterial Spin Labeling

A. Ahlgren[1], R. Wirestam[1], F. Ståhlberg[1,2], L. Knutsson[1]

[1]Dept. of Medical Radiation Physics, Lund University, Lund, Sweden
[2]Dept. of Diagnostic Radiology, Lund University, Lund, Sweden

Introduction

The equilibrium magnetization in arterial blood $M_{0,a}$ is an essential parameter for quantification of Cerebral Blood Flow (CBF) by Arterial Spin Labeling (ASL). $M_{0,a}$ can be estimated by dividing the equilibrium magnetization in tissue $M_{0,t}$ by the brain-blood partition coefficient λ, i.e., $M_{0,a}=M_{0,t}/\lambda$ [1]. The QUASAR implementation [2] is able to map $M_{0,t}$, enabling calculation of $M_{0,a}$ if λ can be determined. Different approaches for the calculation have previously been reviewed [3], and in this study we propose a new method using fractional segmentation.

Subjects and Methods

Volunteers were examined at 3T (Philips Achieva) using the QUASAR sequence [2]: $TR/TE/\Delta TI/TI_1=4000/23/300/40$ ms, 64x64 matrix, 7 slices and 13 inversion times. The new segmentation technique FRActional Signal mapping from InvErsion Recovery (FRASIER) [4] was modified to be applicable to QUASAR data. FRASIER segmented grey matter (GM), white matter (WM) and cerebrospinal fluid (CSF) as normalized fractional signals $f_{s,i}$ and fractional volumes $f_{v,i}$; i=[GM,WM,CSF]. Since there is no arterial blood in the ventricles, λ is not defined in CSF. Therefore, λ can be calculated as a weighted sum of the mean λ in GM (0.98 ml/g) and in WM (0.82 ml/g) [3], i.e., $\lambda_w=f_{v,GM}\cdot\lambda_{GM}+f_{v,WM}\cdot\lambda_{WM}$. $M_{0,t}$ should be corrected for the presence of CSF which is accomplished by using fractional signals, i.e., $M_{0,GM+WM}=M_{0,t}(1-f_{s,CSF})$. $M_{0,a}$ can then be calculated voxel-wise as $M_{0,a}=M_{0,GM+WM}/\lambda_w$.
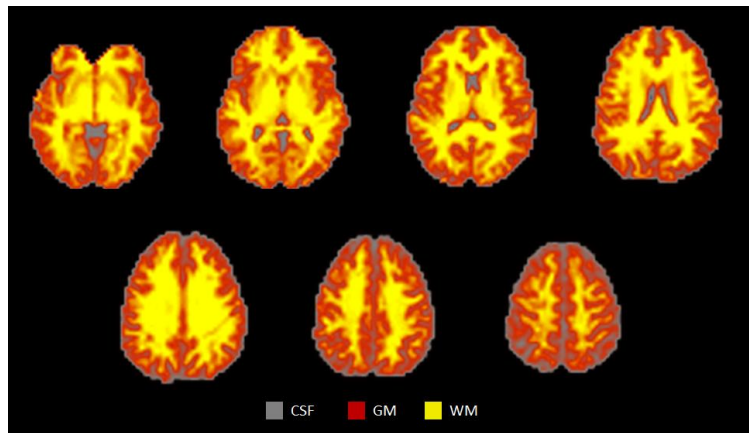

Figure 1. Fractional volumes calculated from saturation recovery data.

Results

Figure 1 shows fractional volumes in one subject. Figure 2 shows $M_{0,GM+WM}$, λ_w, $M_{0,a}$, and $M_{0,a}$ calculated in a traditional manner by dividing $M_{0,t}$ by $\lambda_{GM}=0.98$ ml/g. The mean value of $M_{0,a}$ in GM was consistently higher (n=10, p<0.001) compared to the traditional calculation. Mean values were $(6.05\pm0.25)\cdot10^7$ ml^{-1} for the new method and $(5.99\pm0.25)\cdot10^7$ ml^{-1} for the λ_{GM} method.
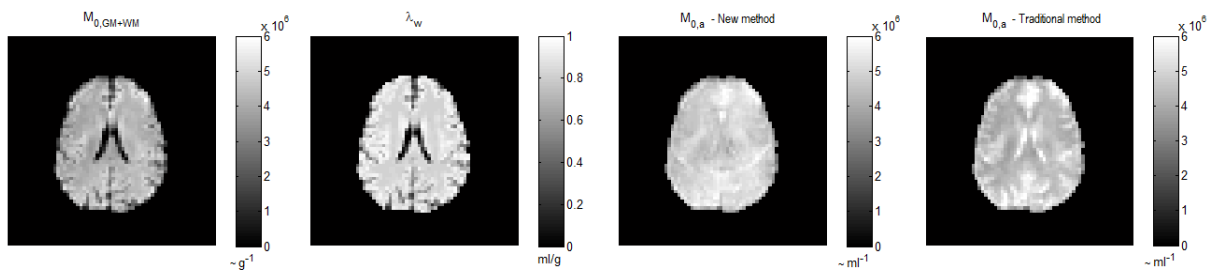

Figure 2. From left to right: $M_{0,GM+WM}$ [~g^{-1}], λ_w [ml/g], new $M_{0,a}=M_{0,GM+WM}/\lambda_w$ [~ml^{-1}] and traditional $M_{0,a}=M_{0,t}/\lambda_{GM}$ [~ml^{-1}].

Discussion

The presented approach is similar to the method in which λ is calculated by linear assignment to tissue T_1 [3], although the new method employs no assumption of linearity. $M_{0,a}$ should include T_2^* changes across the brain, which could be violated as $M_{0,t}$ is altered. However, since T_2^* is long in CSF compared with the parenchyma, the error is likely to be negligible for a TE of 23 ms. The new method takes the definition of λ into account and could improve ASL-based CBF quantification.

References

[1] Detre JA et al., 1992, MRM, 23:37-45. [2] Petersen ET et al., 2006, MRM, 55:219-232. [3] Petersen ET et al., 2006, Proc 14th ISMRM, #2688. [4] Shin W et al., 2010, NeuroImage, 52:1347-1354.